

Controls on carbon isotopes during the upwelling system development in shallow marine environments: Regional evolution in the Roadian (Mid-Permian) of South China

Han Lei ^{a,1}, Wenhui Huang ^{b,*}, Qingchun Jiang ^a, Ping Luo ^a

^a Research Institute of Petroleum Exploration & Development (RIPED), PetroChina, Beijing 100083, China

^b Key Laboratory for Marine Reservoir Evolution and Hydrocarbon Abundance Mechanism, School of Energy Resources, China University of Geosciences, Ministry of Education, Beijing 100083, China



ARTICLE INFO

Editor: Bing Shen

Keywords:

Carbon isotope
Upwelling
Paleoclimate
Sulfate reduction reaction
Shallow marine environments
South China

ABSTRACT

Throughout geological time, upwelling systems have been widespread in shallow marine environments. However, the regional carbon cycle in shallow marine environments during the development of upwelling systems remains unclear. During the middle Permian, astronomically forced upwelling systems were widespread along the west coast of Pangaea and the paleoequator. This study focuses on the astronomical-forced middle Permian (Roadian) rhythmites from the South China continental shelf and carbonate platform to explore the evolution of carbon isotope control factors in shallow marine environments during upwelling system development. Based on geochemical characteristics, time series analyses, and wavelet coherence analyses, the Roadian stage was subdivided into three phases in upwelling system evolution. As the system developed, the continental shelf became oxygen-depleted, warm-humid, and highly weathered, whereas the carbonate platform remained relatively stable. First, the initial development stage. The $\delta^{13}\text{C}_{\text{org}}$ on the continental shelf and the $\delta^{13}\text{C}_{\text{carb}}$ in the carbonate platform averaged $-25.67 \pm 0.57 \text{ ‰}$ and $3.61 \pm 0.25 \text{ ‰}$, respectively. Carbon isotopes in shallow marine environments were primarily controlled by paleoclimate fluctuations (and the upwelling effect). The relatively cool-dry climate weakened continental weathering, upwelling, and organic carbon burial on the continental shelf. However, these conditions also lowered sea levels and restricted water exchange in the carbonate platform, leading to ^{12}C depletion. Next, with the intensification of upwelling, its influence on intra-platform carbon isotopes surpassed paleoclimates, with $\delta^{13}\text{C}_{\text{carb}}$ remaining stable at $3.86 \pm 0.39 \text{ ‰}$. The influx of upwelling during sea-level rise promoted organic carbon burial and a positive shift in $\delta^{13}\text{C}_{\text{carb}}$. On the continental shelf, nevertheless, $\delta^{13}\text{C}_{\text{org}}$ values decreased slightly to $-25.98 \pm 0.61 \text{ ‰}$. The rapid expansion of the oxygen minimum zone reduced sulfate concentrations, facilitating reverse reactions of the anaerobic oxidation of methane and thereby highlighting the control of sulfate reduction reactions on $\delta^{13}\text{C}$. Simultaneously, TS and Fe_{py} contents declined, along with siderite and pyrite deposition. Finally, during the complete development stage, the $\delta^{13}\text{C}_{\text{carb}}$ values in the carbonate platform stabilized at $3.77 \pm 0.45 \text{ ‰}$, while the $\delta^{13}\text{C}_{\text{org}}$ declined to $-26.93 \pm 0.39 \text{ ‰}$. The upwelling intensity and redox conditions gained dominance over ^{12}C by promoting organic carbon burial in shallow marine environments.

1. Introduction

Throughout the Permian, the perturbation of the carbon cycle led to considerable fluctuations in the carbon isotope composition of seawater. During the period of weak volcanic activity, the P1 and P3 glacial episodes of the late Paleozoic ice age (LPIA) triggered positive plateaus in

carbon isotopes at both the Carboniferous–Permian boundary (CPB) and the Cisuralian–Guadalupian boundary (CGB) (Buggisch et al., 2011; Lu et al., 2021; Zhang et al., 2020a). Since the early Capitanian, active oceanic circulation and intensified upwelling have enhanced paleoproductivity and burial of isotopically light organic carbon, resulting in a climatic background of a cooling interval and lowered pCO_2 level, as

* Corresponding author.

E-mail address: huangwh@cugb.edu.cn (W. Huang).

¹ first author

well as a low-latitude eutrophic shallow marine environment, possibly resulting in a positive shift in carbon isotopes within parts of the Paleo-Tethyan domain and Panthalassian realm and preferential losses among warm-water faunas (Isozaki et al., 2011; Nishikane et al., 2014; Zhang et al., 2020a). This transformation is known as the Kamura Event (Isozaki et al., 2007). The Kamura Event concluded in the middle Capitanian, coinciding with the Capitanian biotic crisis and a major global negative carbon isotope excursion, which variously attributed to the onset of the Emeishan large igneous province (ELIP), productivity collapse, oceanic stratification and anoxia, loss of marine habitats due to sea level regression, and catastrophic methane explosions (Bond et al., 2010a; Bond et al., 2010b; Cao et al., 2018; Zhang et al., 2020a). Therefore, prior to the eruption of the ELIP, fluctuations in pCO₂, the waxing and waning of the LPIA, and upwelling were likely closely linked to carbon isotope fluctuations.

The LPIA spans from the Carboniferous to the Permian and comprises eight discrete glacial and nonglacial intervals (Fielding et al., 2023). Generally, global glacial events trigger cooling and weathering attenuation in low-latitude regions (Sun et al., 2023; Yang et al., 2014). Throughout the LPIA, coal forests and silicate weathering might have dominated atmospheric pCO₂ (Cleal and Thomas, 2005; Lu et al., 2021), whereas atmospheric pCO₂ and surface temperature coupling varied with the global ice volume (Lu et al., 2021; Montañez et al., 2016). The P3 glacial episode nearly encompassed the entire Guadalupian Epoch but terminated in the middle Capitanian (Fielding et al., 2023). Intense weathering and the cessation of Kungurian-age large igneous provinces (LIPs) could have been its primary triggers, whereas the continuity of P3 might be attributed to the increased exposure of bedrock in low-latitude regions, thereby sustaining the weathering-driven sequestration of atmospheric pCO₂ (Sun et al., 2023).

During the middle Permian, under the effect of orbital-forced P3 glaciation, the melting of ice sheets induced thermohaline circulation and eutrophicated coastal deep seawater (Beauchamp and Baud, 2002; Beauchamp and Grasby, 2012). Influenced by astronomically forced monsoons or trade winds, upwelling systems developed along the western coasts of Pangea and the paleoequator (Kametaka et al., 2005; Winguth et al., 2002; Yao et al., 2015). In general, an upwelling system forms within continental shelves and slopes, accompanied by oxygen minimum zones (OMZs) (Algeo and Trivelpiano, 2009; Boning et al., 2004; Sweere et al., 2016; Zhang et al., 2022a). Adjacent carbonate platforms were incidentally impacted by upwelling (Lei et al., 2024b). These upwelling systems brought more nutrient-rich deep water to the surface (Montañez and Poulsen, 2013; Zhang et al., 2022a; Zhang et al., 2018). Stratigraphic records in South China suggest that the equatorial upwelling belt intensified during the middle to late Roadian stage (Zhang et al., 2021, 2022a).

In marine environments, various factors, such as seawater temperature affected by atmospheric pCO₂ levels, oceanic circulation, sea level fluctuations, redox conditions, paleoproductivity, and burial and decomposition of organic matter, can collectively influence the composition of carbonate and organic carbon isotopes (e.g., Arthur et al., 1985; Hasegawa, 1997; Meyers, 2014). The establishment of an upwelling system inevitably enhances water exchange and paleoproductivity (e.g., Boning et al., 2004; Liu et al., 2021; Zhang et al., 2022a; Zhang et al., 2018) and could trigger disturbances in the carbon cycle (e.g., Eggleston et al., 2016; Zhang et al., 2022c). In this study, which leveraged the characteristics of astronomical-forced genesis, by geochemical proxies, time series analyses, and wavelet coherence analysis, two sets of middle Permian (Roadian) rhythmites from the carbonate platform and the continental shelf in South China were selected to (1) reconstruct the paleoenvironmental evolution of the shallow marine of South China, and (2) investigate the evolution of carbon isotope control factors, such as paleoclimate conditions, sulfate reduction reactions, and upwelling intensity (redox conditions), in shallow marine environments during upwelling system development. In detail, the Roadian stage comprises three phases in the evolution of the

upwelling system: initial development (Roadian-I), intensification (Roadian-II), and complete development (Roadian-III), which are associated with shifting control factors on carbon isotopes, also manifesting as variations in main cycles in carbon isotopic time series analysis. Furthermore, on the continental shelf, these stages reflect (1) a progressive increase in silicon/carbonate deposition (i.e., the transformation from mudstone to chert-mudstone alternations) and paleoproductivity, (2) intensified upwelling, oxygen depletion, and continental weathering, and (3) a transition toward a warmer, more humid paleoenvironment. The intensification stage is also characterized by decreases in the TS and Fe_{Py} contents and siderite and pyrite depositions and ends with a significant negative shift in carbon isotopes.

2. Geological setting

During the middle Permian, South China was located on the eastern periphery of the Paleo-Tethys Ocean, situated within an equatorial upwelling zone influenced by trade winds (Fig. 1a; Wang and Jin, 2000; Winguth et al., 2002). The paleolatitude ranges from approximately 30° N to 30° S (base map from Ron Blakey, [https://deeptimemaps.com](https://deep timemaps.com)). The South China Block consists of the Yangtze and Cathaysia continents (Li and McCulloch, 1996; Zhang et al., 2020b). Geographically, the Yangtze region is further divided into the Upper Yangtze region to the west and the Lower Yangtze region to the east (Fig. 1b).

Within the Yangtze region, the Upper Yangtze region was occupied primarily by a carbonate platform (Yangtze Carbonate Platform, YCP), whereas the continental shelf was located mainly in the Lower Yangtze region (Fig. 1b) (e.g., Meng et al., 2022; Yao et al., 2015). Since the early Permian, sea levels have experienced a continuous rise. South China was still in transgression in the early Guadalupian Epoch (Zhang et al., 2022b), resulting in the Kangdian old land on the west side reducing its exposed area (Hou, 2020). However, Cathaysia old land in the southeast began to emerge on a large scale due to violent uplift (Hou, 2020). Furthermore, an active margin magmatic arc developed along SE China during the middle-late Permian (Fig. 1b) (Zhang et al., 2022b; Zhang et al., 2020b).

Within the YCP, the Guadalupian Series (middle Permian) corresponds to the Maokou Formation (Fig. 2). The Global Stratotype Sections and Points (GSSPs) for the bases of the Roadian and Wordian stages are defined respectively by the first appearance of *Jinogondolella nankingensis* and *Jinogondolella aserrata* in Guadalupe Mountains National Park, Texas, USA (Glenister et al., 1999; Lambert et al., 2007). In the northwestern Sichuan Basin, the Shangsi section exhibits well-developed and well-preserved Permian strata (Fang, 2012; Fang et al., 2012) and was formerly a candidate section for the GSSP for the Permian–Triassic boundary (Yuan et al., 2019). According to its conodont biostratigraphy, the absence of conodonts before the first occurrence of *J. nankingensis* (Fang et al., 2012), along with a biostratigraphic lag observed for this species in South China (Wang, 2000), indicates that the first appearance of *J. nankingensis* cannot be reliably used to define the base of the Roadian stage (Fang, 2012; Fang et al., 2012) (Fig. 2). Therefore, the contact between LMAs and the underlying limestone with thin mudstone interlayers, corresponding to the contact between limestone–siliceous limestone alternations and siliceous mudstone in the HYX (Huayingxi) section, likely represents the early-middle Roadian stage (Fang, 2012; Fang et al., 2012) (Fig. 2). In addition, the transition from chert–limestone alternations to pure limestone in the Shangsi section represents the terminal Roadian stage (Fang, 2012; Fang et al., 2012) (Fig. 2). However, in the central Sichuan Basin, the Roadian/Wordian boundary is a small-scale unconformity (the Erya section; Peng et al., 2022), corresponding to the boundary of the 1st and 2nd members of the Maokou Formation (hereafter abbreviated as member 1 and member 2) in the HYX section, which is the same unconformity. Therefore, in the HYX section, the top surface of LMAs indicates the Roadian/Wordian boundary (Fig. 2). In the Lower Yangtze region, the Guadalupian Series comprises the Yinping Formation and the underlying Gufeng Formation

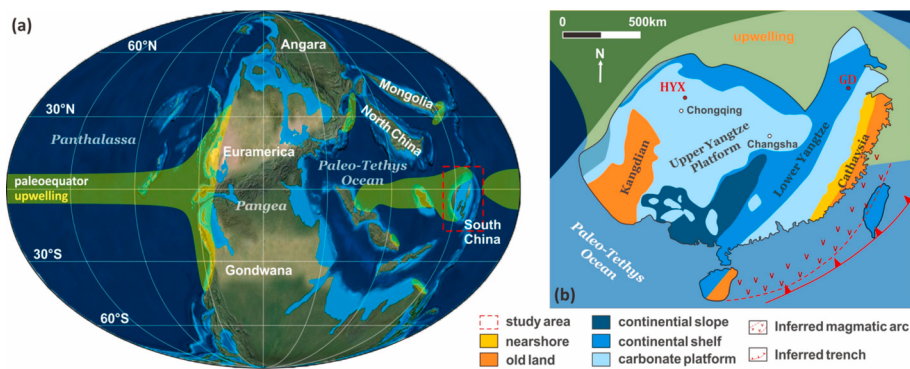


Fig. 1. (a) Global paleogeography of the middle Permian (Guadalupian) (modified from the base map from Ron Blakey, <https://deep timemaps.com>). The yellow shading refers to upwelling systems developed along the west coast of Pangea and the paleoequator (Winguth et al., 2002). The red dotted box highlights the location of the South China Block. (b) Depositional environment of South China (modified from Gao et al., 2020a; Yao et al., 2015). The red spots represent the positions of rhythmites. The location of the magmatic arc refers to Zhang et al. (2022b). (For interpretation of the references to colour in this figure legend, the reader is referred to the web version of this article.)

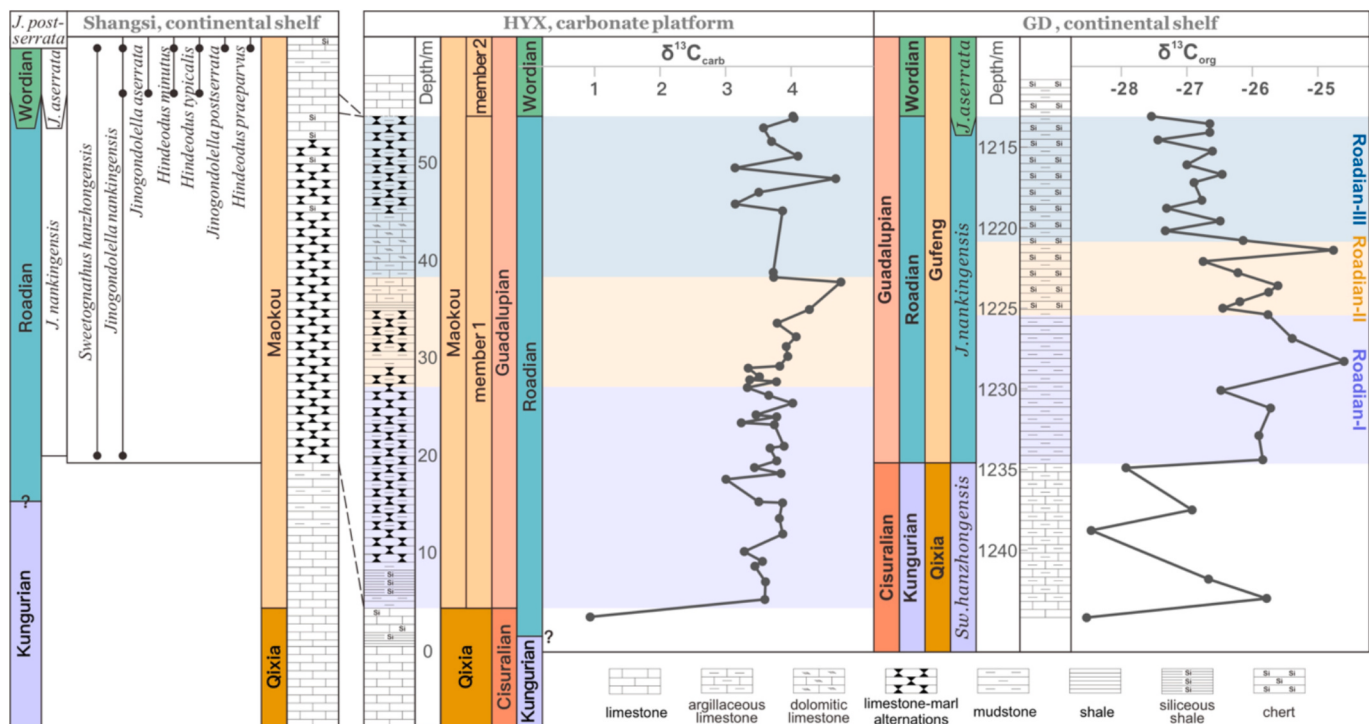


Fig. 2. Stratigraphy and carbonate/organic carbon isotopes of the Roadian strata in the Upper Yangtze carbonate platform and the Lower Yangtze continental shelf (Zhang et al., 2023b). The conodont biostratigraphic characteristics of Shangsi and GD sections are based on Fang (2012), Fang et al. (2012), and Zhang et al. (2023b). Different colors of shaded areas correspond to the initial development of the upwelling system (Roadian-I), intensification of the upwelling system (Roadian-II), and complete development of the upwelling system (Roadian-III). The division of the three phases of the Roadian stage was determined in Section 5.2.

(Fig. 2). The Roadian stage shares the same lower boundary with the Guadalupian Series.

The amalgamation of the Pangea supercontinent initiated the buildup of atmospheric CO₂, leading to ocean acidification along the shallow marine (Beauchamp and Baud, 2002). Ocean acidification triggered the lysocline and the gradual shoaling of calcite compensation depth, which was likely amplified by upwelling (Beauchamp and Grasby, 2012). Siliceous sediments as the substitute occupied deep-water distal areas with the retreat of carbonate factories, which is called the “Permian Chert Event (PCE)” (Beauchamp and Baud, 2002; Murchey and Jones, 1992). In the Yangtze region, silicon-rich rhythmites are deposited as products of the PCE (Lei et al., 2024a; Yao et al., 2015). The YCP is characterized by the development of limestone–marl alternations (LMAs) within the Maokou Formation (e.g., Cai et al., 2019;

Li et al., 2018), whereas the Lower Yangtze region features the occurrence of chert–mudstone alternations in the Gufeng Formation (Zhang et al., 2022a; Zhang et al., 2018). This study involved sampling from the base of the Guadalupian Series to the top of the Roadian stage in both the Sichuan Basin (Huayingxi (HYX) section; Upper Yangtze region) and Anhui Province (Gangdi (GD) section; Lower Yangtze region).

3. Samples, data, and methods

In the YCP, LMAs occupied the member 1, corresponding to 4.8–54.9 m of the HYX outcrop. On the continental shelf of the Lower Yangtze region, mudstone and chert–mudstone alternations of the lower–middle Gufeng Formation correspond to 1213.1–1234.4 m of the GD section (Fig. 2).

Thin sections of LMAs were observed via a LEITZ-CM Leica DM750p optical microscope and CITL CL8200 MK5 cathodoluminescence (CL) device at 15 keV and 0.5 mA at the Key Laboratory for Marine Reservoir Evolution and Hydrocarbon Abundance Mechanism, China University of Geosciences, Beijing. The LMA samples were prepared as milled powders to facilitate subsequent geochemical and isotopic analyses.

3.1. Carbon isotope values

The carbon isotope analyses of 46 LMA samples were conducted using a Finnigan Mat 253 mass spectrometer. Anhydrous phosphoric acid (100 %) in sealed tubes was used to extract CO₂ from 200-mesh rock powder. A phosphoric acid fractionation factor of 1.01025 for calcites was adopted in the calculation of isotopic values (Friedman and O'Neil, 1977). The accuracy and precision of the carbon isotope measurements were monitored via replicate analysis of the NBS19 standard. The reproducibility for the carbon isotope was better than ±0.017 ‰. Organic carbon isotopes of chert–mudstone alterations were referred to Zhang et al. (2020a). They used decarbonated and centrifugated residues extracted from the powdered samples to measure δ¹³C_{org} values, which used continuous flow-elemental analysis-isotope ratio mass spectrometry, with a ThermoFinnigan Deltaplus Advantage mass spectrometer coupled with an EA 1112 Series Flash Elemental Analyzer at the State Key Laboratory for Mineral Deposits Research, Nanjing University. The precision and reproducibility for δ¹³C_{org} were better than ±0.2 ‰. The carbonate and organic δ¹³C values are reported per mil (‰) relative to Vienna Pee Dee Belemnite (VPDB). In the GD section, the δ¹³C_{org} values during the early to middle Roadian stages are relatively high (−26.75 ‰ to −24.6 ‰) and subsequently decrease noticeably during the late Roadian stage (−27.54 ‰ to −26.46 ‰) (Fig. 2).

3.2. Geochemical analyses

Major elemental analyses were performed on powdered whole-rock samples. An AXios-mAmX X-ray fluorescence (XRF) spectrometer was used. The analytical precision was better than 3 %. Trace element and rare earth element (REE) analyses were performed using a PerkinElmer NexION 350 × ICP-MS on digested whole-rock powder samples. Based on analyses of two international rock standards and duplicate samples in each run, the analytical precisions for trace elements and REEs were typically better than 8 % and 10 %, respectively. The acid digestion method was adopted in this study. The powdered samples were digested in a mixture of superpure HNO₃ + HCl + HF in high-pressure Teflon cups (Gao et al., 2015). The total sulfur (TS) content was calculated from the SO₃ content determined by XRF. Moreover, the geochemical data of chert–mudstone alterations were obtained from Zhang et al. (2022a), Zhang et al. (2022b), and Zhang et al. (2023b).

The REE concentrations were normalized to that of post-Archean Australian shale (PAAS; Taylor and McLennan, 1985). The Ce and Eu anomalies are calculated according to Ce/Ce* = Ce_N/[(Pr_N)²/Nd_N] and Eu/Eu* = Eu_N/(Sm_N × (Sm_N/Nd_N)^{1/2}) (Gao et al., 2020a; Wei et al., 2020). The enrichment factor (EF) values (X_{EF} = [(X/Al)_{sample}/(X/Al)_{PAAS}]) and the authigenic fraction (X_{auth} = X_{sample} − Al_{sample}(X/Al)_{UCC}) were utilized, where UCC refers to the composition of the average upper continental crust (McLennan, 2001).

According to the upwelling model of Cd/Mo vs. Co_{EF} × Mn_{EF} (Co × Mn) established by Sweere et al. (2016), a high Cd/Mo value and a low Co_{EF} × Mn_{EF} (Co × Mn) value indicate intensified upwelling. Owing to the possible dilution effect of the large carbonate fractions, the low Al content of LMAs might bias the EFs (Kumpan et al., 2019); thus, the Co × Mn value is utilized instead of the Co_{EF} × Mn_{EF} value. Here, we propose the use of the processed (Co × Mn) × (Cd/Mo)^{−1} values as the upwelling proxy, with lower values indicating intensified upwelling. The upwelling model divides upwelling intensity into three degrees (Sweere et al., 2016). Here, if the same series of samples are distributed at different intensity degrees in the model and if the (Co × Mn) × (Cd/

Mo)^{−1} values of the low-degree samples are lower than those of the high-degree samples, their products should be multiplied by 10 (Table S3).

3.3. Time series analyses

During lifting in the well, the gamma-ray (GR) detector captures natural gamma rays from the stratum and converts them into electrical pulse signals, which are then converted into potential differences through amplifiers and surface instruments, recording them as the natural gamma intensity. Natural gamma-ray logging records the intensity of gamma-rays emitted during the decay of atomic nuclei of the radioactive elements contained in sedimentary rocks. Its intensity is associated with ⁴⁰K, ²³²Th, and ²³⁸U in rocks. Currently, high-resolution natural GR logging data have been widely used in cyclostratigraphic analysis (e.g., Wu et al., 2009; Zhang et al., 2022d). In the central Sichuan Basin, such data from two wells were acquired downhole over the entire cored interval at a spacing of 0.125 m.

Time series analysis was conducted using the Acycle 2.7 program (Li et al., 2019). Based on the time series analysis and sedimentation rate analysis, GR logging data were employed as an accurate framework for detecting the astronomical signals of LMAs. The average sedimentation rates of the member 1 in the two wells of the central Sichuan Basin were 2.77 cm/kyr and 2.74 cm/kyr (Lei et al., 2024b), which were analyzed by correlation coefficient (COCO) method (Li et al., 2019). The COCO method is achieved by combining the correlation coefficient measurements, a Monte Carlo simulation procedure, and the number of contributing astronomical parameters to determine the optimal average sedimentation rate (Li et al., 2019). As an adjacent section of two wells, the average sedimentation rate of the HYX section is assumed to be the average of the two wells (2.755 cm/kyr) because of its lack of GR data (Lei et al., 2024b). The supplementary material provides a statement regarding the feasibility of time series analysis on the middle Permian LMAs of South China. Yao et al. (2015) reported the feasibility of time series analysis of chert–mudstone alternations during the middle Permian. To obtain more reliable main cycles, the data from the GD section were extended to 1205.6–1234.4 m, corresponding to the Roadian to Wordian stages for time series analysis.

The power spectra were computed via the multitaper method (MTM; Thomson, 1982). Frequency analyses were performed with fast Fourier transform (FFT LAH; Kodama and Hinov, 2014) by determining the sliding window lengths and steps, and the results are presented in spectrograms. Frequencies (or wavelengths) were jointly determined from the strongest spectral peaks (with high confidence) in the power spectra and the most stable frequencies in the spectrograms. All the sliding window lengths of the FFT spectrum frequency analyses were determined to be 3 times the maximum value of the most likely wavelengths in the power spectra.

3.4. Wavelet coherence and cross wavelet transform analyses

Wavelet coherence (WTC) and cross wavelet transform (XWT) are widely used to reflect the correlation between two series. WTC finds regions in time (depth) frequency space where the two series covary, which can reflect the correlation between variations in the two series. The XWT finds regions in time (depth) frequency space where the series shows high common power, which generally reflects the power of the common cycle between series. In the wavelet graph, yellow highlights the sections with a correlation between variations in the two series. The right arrow represents in-phase signals, and the left arrow represents antiphase signals. The downward arrow indicates that the first series varies ahead of the second series, whereas the upward arrow indicates that the first series varies behind the second series.

4. Results

4.1. Petrological characteristics

In the member 1 of the HYX section (Fig. 2), thin mudstone and shale layers developed at the base, followed by a thick interval of LMAs. The LMAs are subsequently interbedded within thin layers of mudstone and shale. Finally, argillaceous limestones and dolomitic limestones overlie the LMAs. LMAs consist of limestone nodules and encased marls. Limestone nodules, which typically range from 15 to 20 cm in length, are most common, whereas the thickness of the marl layers varies from 5 to 35 cm.

In the Roadian stage of the GD section, the lithology comprises mudstone from the lower Gufeng Formation and chert–mudstone alternations from the middle Gufeng Formation (Fig. 2). Chert is classified morphologically into bedded and nodular chert. Bedded chert commonly occurs in thin layers, whereas nodular chert is typically found as nodules or bands (Kametaka et al., 2005; Yao et al., 2015; Zhang et al., 2023a). The GD section is characterized by bedded chert (Zhang et al., 2023b).

4.2. Carbon isotope and geochemical compositions

4.2.1. Carbon isotope composition

For both the carbonate platform and the continental shelf, the base of the studied interval presented the lowest carbon isotope values, followed by a pronounced positive shift in $\delta^{13}\text{C}$ (Fig. 2). Within the carbonate platform, apart from the basal samples, the $\delta^{13}\text{C}_{\text{carb}}$ values range from 3.01 ‰ to 4.76 ‰.

4.2.2. Geochemical composition

On the continental shelf, significant disparities typically exist in the ranges of various geochemical proxies between the Roadian-I stage and the Roadian-II/III stage (Table S1). However, in the carbonate platform, the geochemical proxies may fluctuate significantly but do not exhibit phased (Table S2).

The Si/Ca ratio is used to characterize the alternation of silicon/carbonate deposition in this study but also likely signifies weathering intensity on the continental shelf. On the continental shelf, the Si/Ca ratio ranges from 0.51 to 4.42 during the Roadian-I stage, whereas the ratio during the Roadian-II/III stage ranges from 4.92 and 113.00. In the carbonate platform, the Si/Ca ratio fluctuates between 0.046 and 38.008.

The Cd/Mo value, the Co \times Mn value, and the upwelling proxy are applied to determine the upwelling intensity (Sweere et al., 2016; Table S3). Moreover, Fang et al. (2018a) proposed that the periodic variations in the Ba/Ti ratios of the Maokou strata (lithologies include LMAs, chert, and mudstone) respond well to Milankovitch-forced nutrient availability in the surface ocean due to the effect of upwelling in South China, with an increasing ratio indicating an increased nutrient supply. On the continental shelf, during the Roadian-I stage, the Cd/Mo value is 13.09 ± 8.89 , the Co \times Mn value is 3.85 ± 4.02 , and the Ba/Ti ratio is 0.070 ± 0.017 , whereas during the Roadian-II/III stage, the values are 0.55 ± 0.19 , 0.11 ± 0.26 , and 0.148 ± 0.098 , respectively. In the carbonate platform, the Cd/Mo value and the Co \times Mn value are 1.64 ± 2.31 and $0.92 \pm 1.43 (\times 10^{-3})$, respectively. The Ba/Ti ratio is 0.16 ± 0.45 .

As marine micronutrients, Cu, Ni, and Zn are widely used as paleoproductivity proxies (e.g., Algeo and Maynard, 2004; Tribouillard et al., 2006). Generally, they are delivered to the sediment mainly in association with organic matter as organometallic complexes and are preserved in the sediment in the form of sulfides after the decomposition of organic matter under reducing conditions (Algeo and Maynard, 2004;

Tribouillard et al., 2006). Here, we use Ni_{auth}, which rules out the influence of detrital dilution, to reconstruct paleoproductivity changes. On the continental shelf, the Ni_{auth} value during the Roadian-I stage is 59.21 ± 28.51 , whereas the value during the latter stage is 152.14 ± 62.95 . In the carbonate platform, the Ni_{auth} value is 3.53 ± 2.80 .

The weathering index of Parker (WIP) value, the chemical index of alteration (CIA) value, the K₂O/Al₂O₃ ratio, and the Al/Ti ratio serve as chemical weathering indicators (Nesbitt and Young, 1982; Parker, 1970; Shao et al., 2012; Westphal et al., 2010; Zhang et al., 2022a). On the continental shelf, the WIP value and the CIA value during the Roadian-I stage are 33.20 ± 5.37 and 75.74 ± 1.03 , respectively, whereas during the latter stage, they are 8.38 ± 5.79 and 78.77 ± 5.55 , respectively. In the carbonate platform, the K₂O/Al₂O₃ ratio and the Al/Ti ratio are 0.20 ± 0.12 and 11.50 ± 3.26 , respectively.

Most interpretations of the marine carbonate Ce anomaly (Ce/Ce*) assume that a negative Ce anomaly indicates an oxic or suboxic depositional environment and that a positive Ce anomaly indicates an anoxic depositional environment (Cao et al., 2020). To accurately assess paleoredox conditions in the marine environment, it is important to evaluate the hydrogenous REEs present in authigenic fractions, as the Ce/Ce* ratios of solid-phase sediments, which are affected by REEs from detrital fractions, may not provide precise indications (Chen et al., 2015; Gao et al., 2020b). We selected LMA samples from the central Sichuan Basin (HYX and X2; X2 is located west of HYX in the central Sichuan Basin) to apply the $\Sigma\text{REE}/\text{Th}$ vs. Y/Ho model (Fig. 3a; modified from Chen et al., 2015; Gao et al., 2020b). Most samples plot left of the trend line, which is likely due to the metasomatism of authigenic siliceous minerals (Mg-phyllosilicates and quartz) on carbonate minerals (Lei et al., 2022; their contents show negative correlations, $R^2 > 0.9$), causing diagenetic loss of REEs and significant depletion of $\Sigma\text{REE}/\text{Th}$. The diagram (Fig. 3a) shows that LMAs basically maintain the initial seawater signal of REEs. Therefore, Ce/Ce* is a reliable proxy for the paleoredox analysis of LMAs.

Moreover, although the redox proxies proposed by Jones and Manning (1994), such as bimetal ratios including V/Cr and Ni/Co, have been widely applied, the performance of bimetal ratios as redox proxies is far inferior to that of trace metal enrichment factors (EFs) (Algeo and Liu, 2020; Piper and Calvert, 2009). By assessing enrichment factors, authigenic Mo–U covariation (Mo_{auth}/U_{auth} ratio) can yield information concerning variation in benthic redox conditions (Algeo and Tribouillard, 2009; Zhang et al., 2021). However, the EFs of LMAs could be biased due to their low Al contents. Therefore, we employed principal component analysis (PCA) between the Ce/Ce* value, Mo_{EF} value, U_{EF} value, V_{EF} value, (Mo/U)_{auth} ratio, V/Cr ratio, and Ni/Co ratio for LMAs. PCA is a classic ordination method and refers to a statistical technique that linearly transforms an original set of variables into a substantially smaller set of uncorrelated variables (principal components, PCs) that represents most of the information in the original set of variables (Dunteman, 1989). This method can decipher the relationships between Ce/Ce* and multiple potential redox proxies. In the PCA results of both the HYX and X2 LMAs, only the (Mo/U)_{auth} ratio is closely associated with Ce/Ce* (Fig. 3b), indicating its good performance as a redox proxy for LMAs. In the carbonate platform, the Ce/Ce* value and (Mo/U)_{auth} ratio are 0.70 ± 0.20 and 0.56 ± 0.53 , respectively. For the GD section, the Ce anomalies require recovery of a hydrogenous signal, and thus, cannot be applied to shales (Algeo and Liu, 2020). Previously, the Mo_{EF} value, V_{EF} value, and TOC/TP ratio have been proven to have well-recorded variations in the paleoredox conditions of the mid-Permian stratum in the GD section (Zhang et al., 2021; Zhang et al., 2022a). On the continental shelf, during the Roadian-I stage, the Mo_{EF} value, V_{EF} value, and TOC/TP ratio are 1.19 ± 0.72 , 1.83 ± 0.89 , and 15.57 ± 5.47 , respectively. During the Roadian-II/III stage, these values are 421.69 ± 447.01 , 18.42 ± 13.47 , and 653.08 ± 345.30 , respectively.

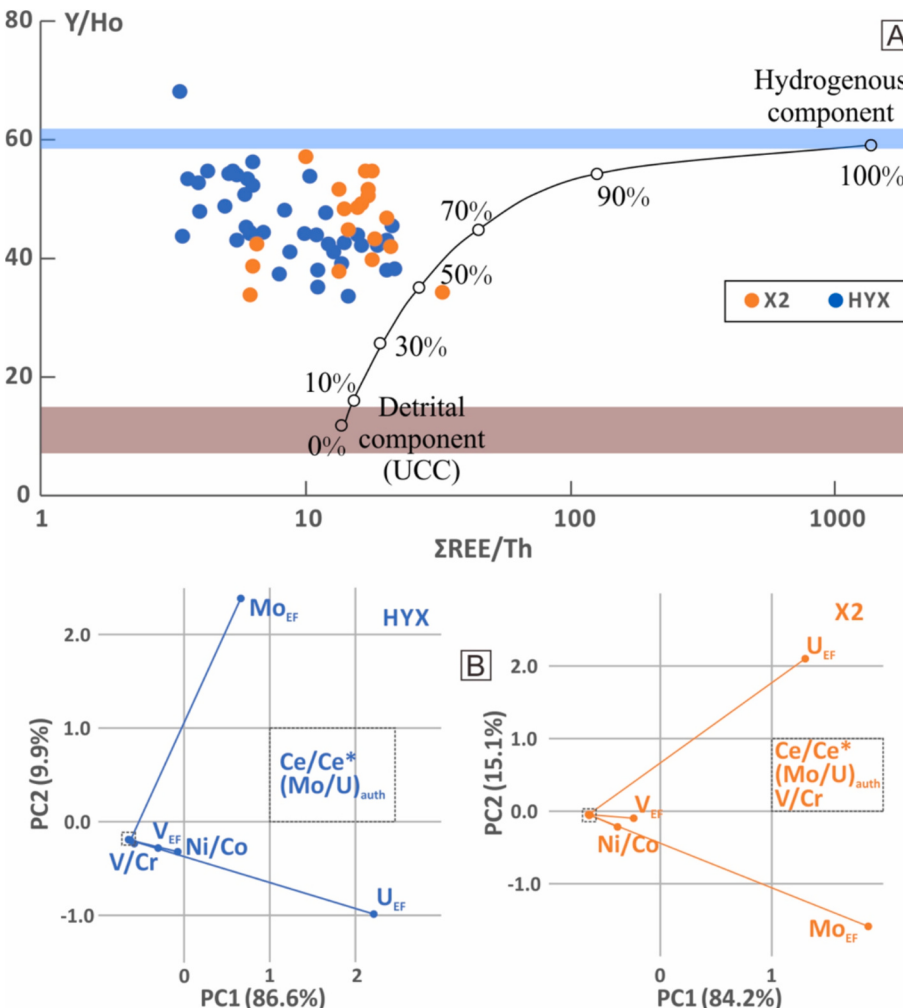


Fig. 3. (a) Y/Ho vs. $\Sigma\text{REE}/\text{Th}$ model. The curve represents a mixed trend between the hydrogenous component and the detrital component with the UCC composition (McLennan, 2001), with the percentage of the hydrogenous component provided (Chen et al., 2015). (b) Principal component analysis (PCA) results between the Ce/Ce^* value, the V/Cr , Ni/Co , and $(\text{Mo}/\text{U})_{\text{auth}}$ ratios and the Mo_{EF} , V_{EF} , and U_{EF} values for LMAs. X2 is a well core in the central Sichuan Basin, west of the HYX section.

The CIA value, Ga/Rb ratio, and the Sr/Cu ratio are used to characterize paleoclimate conditions (Li et al., 2021; Roy and Roser, 2013; Sarki Yandoka et al., 2015; Stüben et al., 2002; Zhang et al., 2021). On the continental shelf, during the Roadian-I stage, the Sr/Cu ratio is 23.84 ± 14.07 . During the Roadian-II/III stage, the ratio is 3.75 ± 4.00 . In the carbonate platform, the Ga/Rb ratio is 0.12 ± 0.10 .

4.3. Time series analyses

4.3.1. Continental shelf (GD section)

With respect to the organic carbon isotope series, the power spectrum and frequency analysis reveal six potential main cycles within the Roadian stage (1213.1–1234.4 m), including wavelengths of 5.25 m, 4.2 m, 3.59 m, 2.53 m, 2.13 m, and 1.81 m (Fig. 4). However, owing to the absence of the average sedimentation rate in this section, these cycles (m) cannot be correlated with the known astronomical cycle (kyr).

The above cycles of the organic carbon isotope series can also be detected in multiple proxies (Fig. 4). In the Si/Ca ratio series, two main cycles with wavelengths of 3.5 m and 1.99 m are revealed within the Roadian stage. Wavelengths of ~ 4.46 m, ~ 3.54 m, and ~ 2.04 m with strong signals are detected in the upwelling proxy series and the TOC content series within the Roadian stage. The TOC content series also displays a main cycle with a wavelength of 1.79 m. Within the Roadian

stage, the Ni_{auth} value series, the TS content series, the TOC/TP ratio series, and the Fe_{py} content series display three main cycles at wavelengths of ~ 5.55 m, ~ 4.39 m, and ~ 3.66 m. Moreover, the main cycles of the TOC/TP ratio series include 2.01 m. The main cycles of the Fe_{py} content series include 2.13 m and 1.91 m.

4.3.2. Carbonate platform (HYX section)

In a previous study focusing on the middle Permian rhythmites of South China, we identified and elucidated two ~ 200 -kyr cycles associated with short eccentricity cycles, including ~ 210 -kyr and ~ 180 -kyr cycles (Lei et al., 2024b). The ~ 210 -kyr cycle was recognized as the pivotal astronomical cycle for upwelling in South China during the mid-Permian (Lei et al., 2024b).

Within the carbonate carbon isotope series, the power spectra display three identical strong peaks (Fig. 5). The wavelengths of 5.95 m and 5.21 m correspond to the ~ 210 -kyr and ~ 180 -kyr cycles, respectively, whereas the wavelength of 3.52 m corresponds to the ~ 123 -kyr short eccentricity cycle.

Regarding the Si/Ca ratio, the Al/Ti ratio, the upwelling proxy, the TS content, the Ni_{auth} value, the $(\text{Mo}/\text{U})_{\text{auth}}$ ratio, and the Ga/Rb ratio, their spectrograms reveal two stable frequencies associated with strong spectral peaks at wavelengths within the ranges [5.80, 6.58] m and [5.00, 5.30] m (Fig. 5). These wavelengths correspond to the ~ 210 -kyr

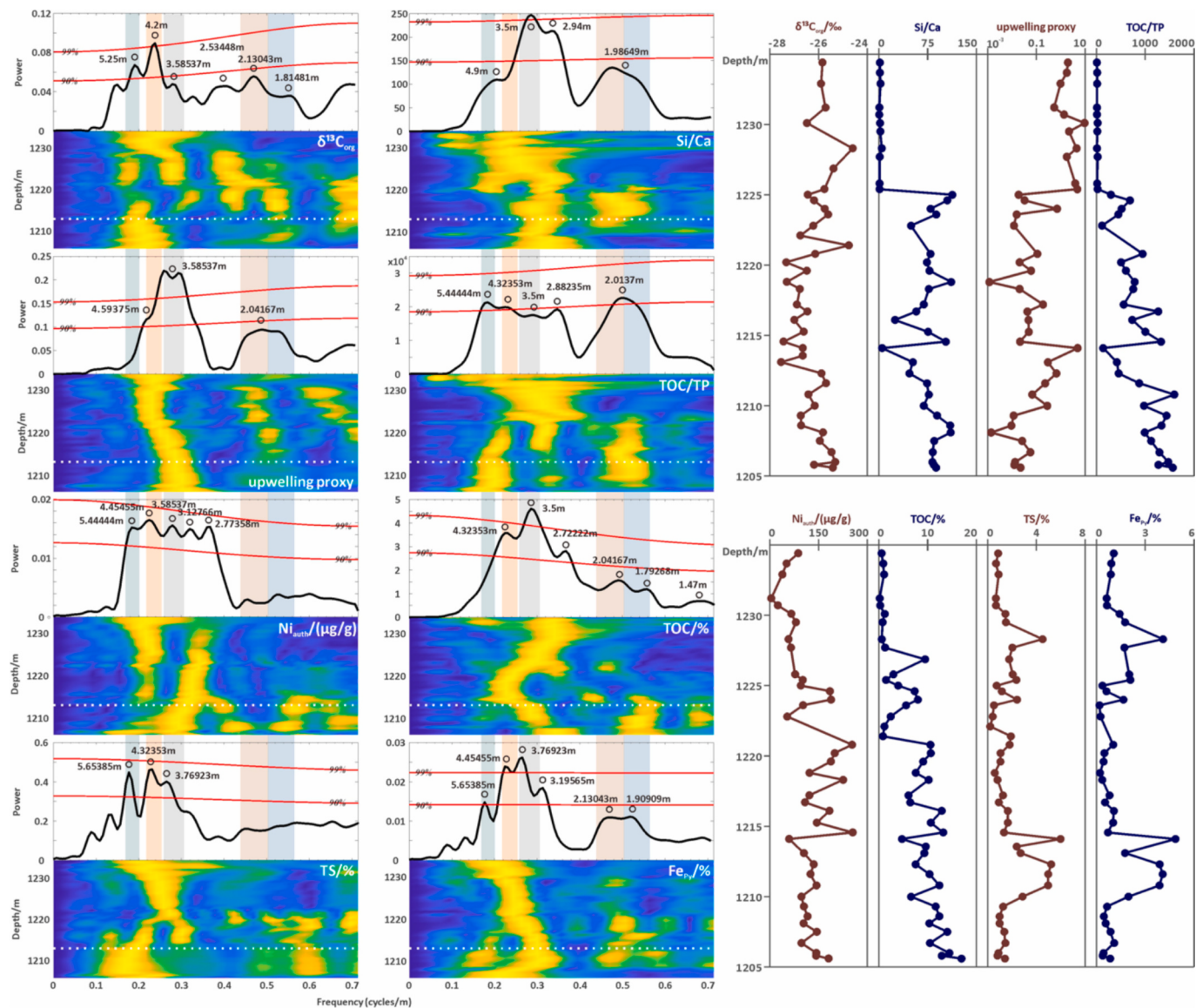


Fig. 4. Time series analyses of various proxies from the GD section (mudstone and chert–mudstone alternations, continental shelf, Lower Yangtze region). The shading highlights the main cycles detected from these proxies. However, owing to the absence of the average sedimentation rate in this section, these cycles (m) cannot be correlated with the known astronomical cycle (kyr). Left: 2π MTM power spectra and spectrograms; Right: trends of various proxies.

and ~ 180 -kyr cycles. Moreover, the ~ 95 -kyr short eccentricity cycle is detected from the Al/Ti ratio, the $(\text{Mo}/\text{U})_{\text{auth}}$ ratio, and the Ni_{auth} value series, with a primary wavelength of 2.6–2.7 m.

5. Discussion

5.1. Reliability of carbonate carbon isotopes and the source of organic carbon

Generally, modification of diagenetic fluids can increase the Fe and Mn contents of calcites, resulting in their strong CL luminescence (Anderson and Arthur, 1983; Lan et al., 2015). However, the micritized calcareous components in the LMA sample remain in dim brownish-red under microscope CL (Fig. 6a~c), indicating they formed in a marine phreatic environment and preserved the primary marine characteristics (Lan et al., 2016; Li et al., 2016). At the top of the member 1, sporadic dolomites are distributed within LMAs (Fig. 6d). Wang et al. (2022) considered that such dolomite was formed through incomplete dolomitization of calcareous sediments. Although dolomitized samples have

slightly higher REE contents than marine limestones, they still maintain similar geochemical character as marine limestones, such as a leftward incline in the REY patterns, high Sr and Ca contents, and low Fe and Mn contents (Wang et al., 2022). Therefore, even if a few surface or atmospheric water participated in dolomitization, the relevant samples can still reflect the characteristics of seawater (Wang et al., 2022). Moreover, the Fe contents of the above samples are below 1% (Fig. 6a~d); thereby, there is no quenching effect on carbonate minerals in CL observations (Pierson, 1981).

The Mn/Sr ratios of the Roadian LMAs are significantly less than 0.1 (0.013 ± 0.005). The $\delta^{13}\text{C}$ values of Guadalupian brachiopods range from 2.9 ‰ to 5.04 ‰ (Korte et al., 2005), and the $\delta^{13}\text{C}$ value of the Roadian marine carbonate rock ranges from approximately 2.84 ‰ to 5.53 ‰ (Frank et al., 2008). The $\delta^{13}\text{C}_{\text{carb}}$ values of the HYX section ($3.72\text{ ‰} \pm 0.36\text{ ‰}$) are distributed within these intervals. Moreover, the $\delta^{18}\text{O}$ values range from -7.70 ‰ to -5.07 ‰ , which are higher than -8 ‰ , and do not correlate with the $\delta^{13}\text{C}_{\text{carb}}$ values ($R^2 = 0.0019$; Fig. 6e). Therefore, the Roadian LMAs retain primary seawater characteristics, and their carbon isotopes are not significantly modified during

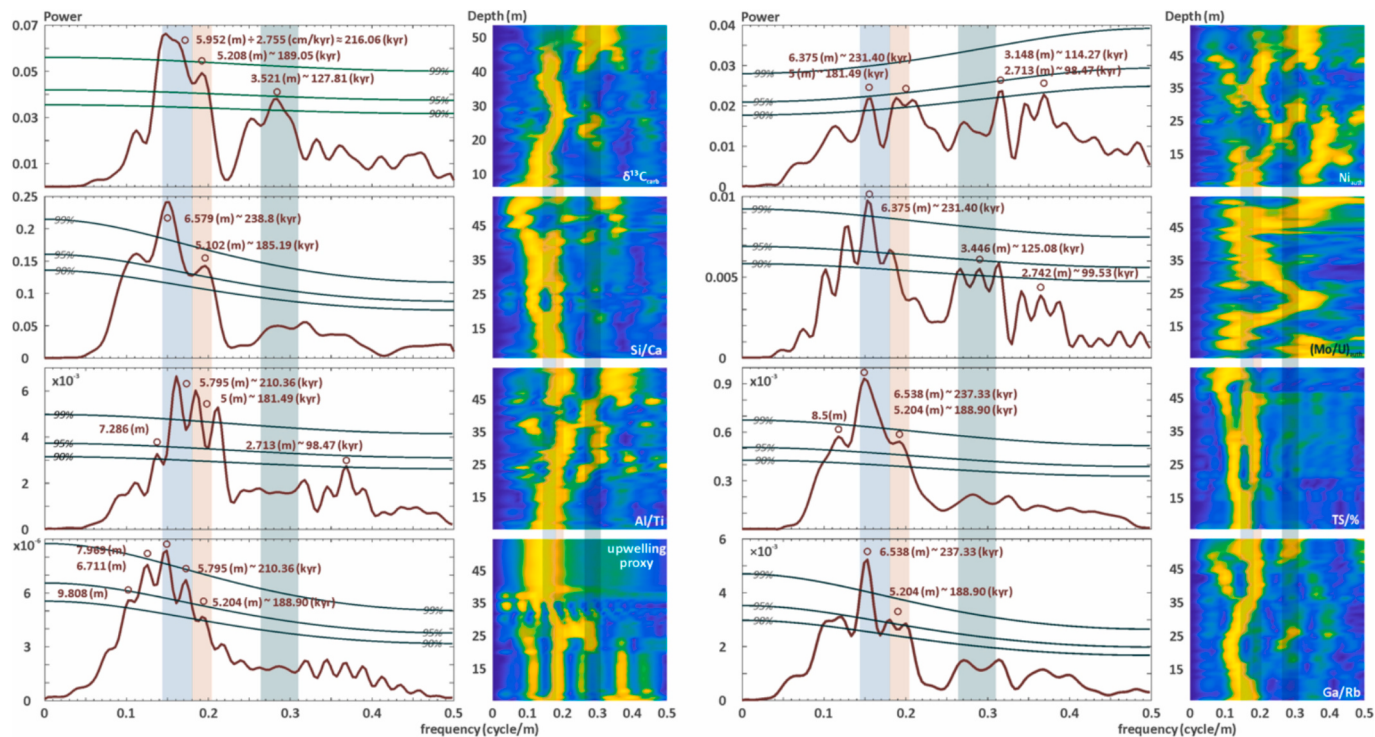


Fig. 5. Time series analyses of various proxies from the HYX section (LMAs, carbonate platform, Upper Yangtze region). The average sedimentation rate is 2.755 cm/kyr (Section 3.3; Lei et al., 2024b). The shading highlights the ~210-kyr, ~180-kyr, and ~123-kyr short eccentricity cycles detected from these proxies. Left: 2π MTM power spectra; Right: spectrograms.

diagenesis (Jacobsen and Kaufman, 1999; Knauth and Kennedy, 2009; Veizer et al., 1999).

For marine sediments, the organic carbon isotopic composition can be affected by the changing contributions of terrestrial and marine organic carbon (Hayes et al., 1999; Meyers, 1997). Therefore, evaluating the source of organic carbon is important. During the late Paleozoic era, the carbon isotope values of marine organic matter ranged from -25‰ to -30‰ , and those of terrestrial organic matter ranged from -22‰ to -24‰ (Zhang et al., 2020a). The organic carbon isotope value of the Roadian stage in the GD section is $-26.32\text{‰} \pm 0.75\text{‰}$. The Al content is not correlated with organic carbon isotopes ($R^2 = 0.0713$; Fig. 6f). Furthermore, palynofacies analysis demonstrates that the organic matter of the Gufeng samples in GD lacks palynomorphs and was predominated by amorphous organic matter (81 % ~ 91 %) (Zhang et al., 2020a), which is typically derived from phytoplankton or is of bacterial origin (Tyson, 1994). Quantitative organic petrographic observations show that the dominant maceral composition of the Gufeng Formation is sapropelinite mainly presenting as micrinized amorphous organic matter with only a few inertites observed (Zhang et al., 2022a). The kerogen type index of the Gufeng Formation calculated by the maceral contents ranges from 41.7 to 90.6 (Zhang et al., 2022a), meeting the standard of type I and II_I kerogen (PRC National Energy Administration, 2014). Therefore, the organic matter preserved in the Roadian stage of the GD section was predominantly of marine origin, and its organic carbon isotopes showed minimal influence from terrestrial organic carbon.

5.2. Paleoenvironmental reconstructions of the shallow sea in South China during the Roadian stage

In the shallow marine of South China, three phases of the Roadian stage correspond to shifts in the correlations between multiple proxies and carbon isotopes (Fig. 8) and nodes of signal power alteration (Figs. 4 and 5). In addition, the continental shelf exhibits significant variations

in paleoenvironment and paleoclimate characteristics, while the carbonate platform keeps in a relative steady condition (Fig. 7).

5.2.1. Redox conditions

Mo is usually enriched under H_2S -rich euxinic conditions and decreases concentration with the weakening of oxygen depletion (Algeo and Tribouillard, 2009). U is preferentially enriched in sediments underlying anoxic/euxinic conditions, but Mo_{auth} is always progressively more enriched than U_{auth} (Algeo and Maynard, 2004; Algeo and Tribouillard, 2009; Fujisaki et al., 2016). Therefore, the Mo_{auth}/U_{auth} ratio of <0.9 ($0.3 \times \text{SW}$), $0.9\text{--}3$ ($0.3\text{--}1 \times \text{SW}$), $3\text{--}9$ ($1\text{--}3 \times \text{SW}$), and >9 ($3 \times \text{SW}$) indicates oxic-suboxic, weakly anoxic, strongly anoxic-euxinic, and euxinic conditions in the middle Permian sediments, respectively (Algeo and Tribouillard, 2009; Zhang et al., 2021). Moreover, under anoxic conditions, insoluble Ce⁴⁺ is generally reduced to soluble Ce³⁺. Hence, the Ce anomaly (Ce/Ce*) is a reliable indicator of paleoredox conditions in paleo-oceans (Wright et al., 1987). As a redox-sensitive trace element, V is present in soluble forms under oxic conditions and is converted to insoluble forms under suboxic-euxinic conditions (Tribouillard et al., 2006). Therefore, it is enriched relative to AUCC under oxygen-depleted conditions and has been widely used to evaluate redox conditions (e.g., Tribouillard et al., 2006; Zhang et al., 2022a). In addition, the TOC/TP molar ratio has been proven useful for reflecting the redox conditions of water columns and bottom sediments (Algeo and Ingall, 2007; Arthur and Sageman, 1994). Generally, a TOC/TP ratio of <50 indicates oxic conditions, 50–100 indicates suboxic conditions, and >100 indicates anoxic conditions (Algeo and Ingall, 2007).

On the shelf, the V_{EF} value maintains increasing and the TOC/TP ratio increases from less than 50 to greater than 100 from the Roadian-I to Roadian-II/III stages, indicating a transformation from oxic to anoxic conditions during the formation of the OMZ within the upwelling system (Fig. 7a). In contrast, there is no significant variation in the range of the redox proxies on the carbonate platform. The Ce/Ce* values and (Mo/U)_{auth} ratios predominantly fall within the ranges of 0.5 to 1.0 and 0 to

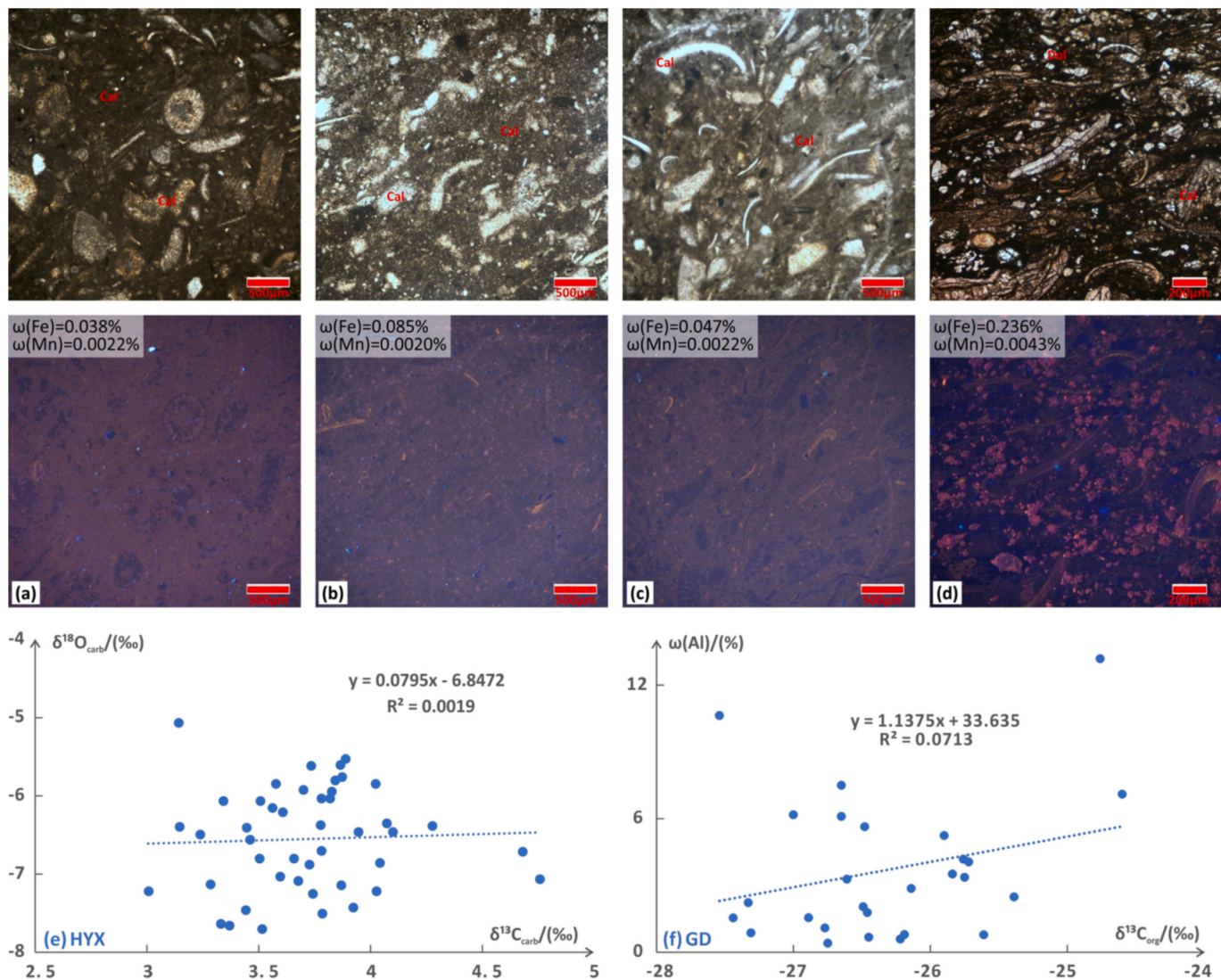


Fig. 6. (a) HYX, 8.8 m, marl, (above) single-polarized light, and (below) optical microscope CL. (b) HYX, 21.1 m, argillaceous limestone, (above) single-polarized light, and (below) optical microscope CL. (c) HYX, 13.7 m, limestone, (above) single-polarized light, and (below) optical microscope CL. (d) HYX, 54.7 m, dolomitic marl, (above) single-polarized light, and (below) optical microscope CL. (e) Crossplot of $\delta^{13}\text{C}_{\text{carb}}$ vs $\delta^{18}\text{O}_{\text{carb}}$ in the HYX section. (f) Crossplot of $\delta^{13}\text{C}_{\text{org}}$ vs. Al content in the GD section.

0.9, respectively; indicating that the carbonate platform remains in an oxic to suboxic environment (Fig. 7a). However, in the central Sichuan Basin, the rims of Mg-phyllosilicate are often metasomatized by pyrite, leading to a local response to Mo enrichment in pyrite-bearing sepiolite rims (Gao et al., 2020a). Therefore, there could be a severe decrease in the bulk Mo content of LMAs (Lei et al., 2024b). The YCP could be more oxygen-depleted than the proxies show.

5.2.2. Continental chemical weathering and paleoclimate

For chert and mudstone, the CIA value can be effectively used to determine the degree of weathering in the source area (Zhang et al., 2021). The WIP is a reliable proxy for evaluating the weathering intensity of silicate rocks based on the proportions of alkali and alkaline earth elements in weathered products (Parker, 1970; Shao et al., 2012). Regarding LMAs, the ratio of inert elements, such as the Al/Ti ratio, is the prime weathering index, reflecting differences in the weathering intensity of the hinterland between limestones and marls (Westphal et al., 2010). Moreover, elements such as Al and K are rarely influenced by biogenic or diagenetic processes and have thus been widely used as detrital influx indicators (Tribovillard et al., 2006). The K₂O content of LMAs is positively correlated with the content of Al₂O₃ ($R^2 = 0.6033$,

indicating the detrital origin of K. Therefore, the K₂O/Al₂O₃ ratio can be a weathering indicator for LMAs (Zabel et al., 2001; Zhao and Zheng, 2015). Generally, increases in the CIA value and Al₂O₃/TiO₂ ratio and decreases in the WIP value and K₂O/Al₂O₃ ratio indicate intensified chemical weathering.

When the CIA value is used for a paleoclimate proxy, CIA values ranging from 65 to 80 reflect a warm and humid climate and from 80 to 100 suggest a hot and humid climatic condition (Nesbitt and Young, 1982). Common indicators for paleoclimate analysis include Ga/Rb and Sr/Cu ratios (Li et al., 2021; Roy and Roser, 2013; Sarki Yandoka et al., 2015). Generally, Ga is associated with fine-grained aluminosilicate and kaolinite, whereas Rb is linked to illite (Roy and Roser, 2013). Under warm and humid conditions, the precipitation of Sr (as SrSO₄) gradually decreases (Li et al., 2021). Therefore, a high Ga/Rb value indicates warm and humid climates (Beckmann et al., 2005; Roy and Roser, 2013). The Sr/Cu ratio of 1.3–5.0 indicates a warm and humid climate; over 5.0 reflects drought conditions (Lv et al., 2022). However, riverine runoff (continental weathering) and hydrothermal fluids could affect Sr in marine chert and mudstone (Elderfield, 1986). In oxygen-depleted conditions, Cu can form sulfides by combining with H₂S and be stored in sediments (Tribovillard et al., 2006). On the continental shelf, Sr

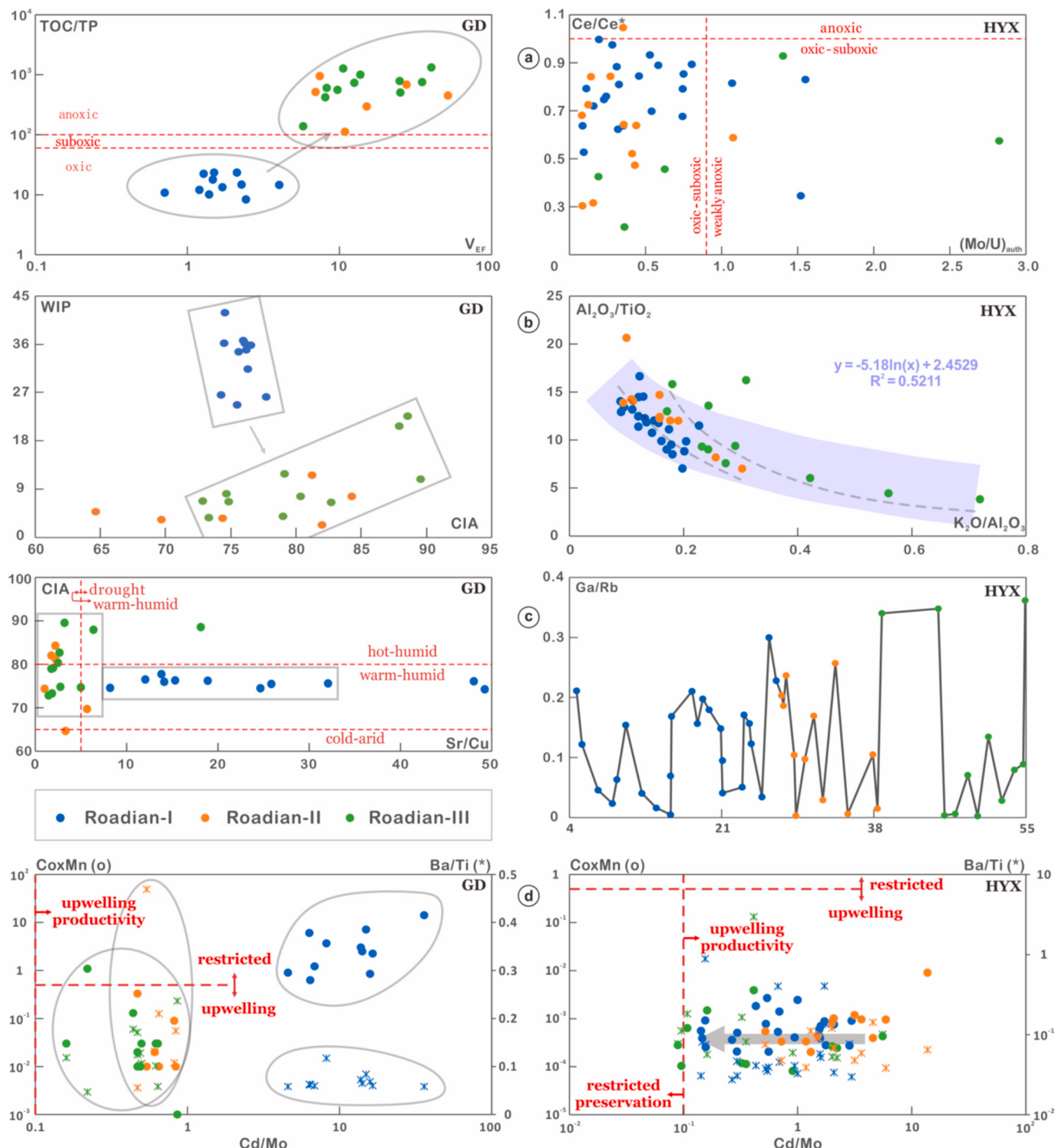


Fig. 7. Paleoenvironmental variations in the shallow marine environment during the development of the upwelling system. (a) Redox condition analyses: plot of V_{EF} values vs. TOC/TP ratios and $(Mo/U)_{auth}$ ratios vs. Ce/Ce^* values. (b) Weathering intensity analyses: plots of CIA values vs. WIP values and K_2O/Al_2O_3 ratios vs. Al_2O_3/TiO_2 ratios. (c) Paleoclimatic analyses: trends of Sr/Cu ratios, CIA values, and Ga/Rb ratios. (d) Upwelling model: Co × Mn values (and Ba/Ti ratios) vs. Cd/Mo ratios (Fang et al., 2018b; Sweere et al., 2016).

contents correlate with WIP values ($R^2 = 0.74$) and Cu contents lack correlation with redox proxies ($R^2(V_{EF}) = 0.04$, $R^2(Mo_{EF}) = 0.04$, and $R^2(TOC/TP) = 0.34$). Therefore, the Sr/Cu ratio likely indicates continental weathering intensity better than paleoclimate conditions.

From the Roadian-I to Roadian-II/III stages on the continental shelf, the WIP value significantly decreases, the CIA value increases from a

narrow range of 75.74 ± 1.03 to a wide range of 78.77 ± 6.89 , and the Sr/Cu ratio declines to approaching or below the threshold of 5.0 (Fig. 7b and c). In the carbonate platform, the Ga/Rb ratios fluctuate within a stable range and the K_2O/Al_2O_3 (Al_2O_3/TiO_2) ratio only exhibits a slight increase (decrease) during the Roadian stage (Fig. 7b and c). Therefore, the continental shelf became warmer and more humid and

experienced more intensified chemical weathering at the Roadian-II/III stage. However, there was no significant change in the paleoclimate of the contemporaneous carbonate platform with only a slight weakening of chemical weathering (Fig. 7b and c).

5.2.3. Upwelling and eutrophic seawater

The combined use of the Cd/Mo and Co × Mn proxies can be utilized to reflect the impact of upwelling on the shallow sea (Sweere et al., 2016). Mn is deficient in upwelling systems with OMZs (Brumsack, 2006; Tribouillard et al., 2006), whereas the outflow of dissolved riverine Mn is limited in restricted environments (Sweere et al., 2016). Co exhibits a cycling behavior similar to Mn (Boning et al., 2004; Sweere et al., 2016). Thus, Co and Mn deficiencies are characteristic features of coastal upwelling sediments with Co × Mn values <0.4 (Sweere et al., 2016). In upwelling systems, substantial plankton fluxes are likely to induce high productivity and significant Cd enrichment (Conway and John, 2015). The limited impact of biological uptake on Mo leads to its enrichment in restricted environments (Algeo and Lyons, 2006). Thus, a Cd/Mo ratio cutoff of ~0.1 can distinguish organic-rich sediments from productivity-driven upwelling settings and preservation-driven restricted basins (Sweere et al., 2016).

Ba is produced from barite (Dymond et al., 1992) and is stable under the effect of diagenesis in oxic sediments (Dehairs et al., 1991). Ti-normalized Ba can eliminate the dilution effect of biogenic and authigenic elements and therefore can be used to identify the authigenic enrichment of Ba in marine sediments (Murray et al., 2000). Generally, high Ba fluxes (Ba/Ti ratios) indicate high surface productivity and nutrient levels (Fang et al., 2018a), corresponding to an intensified upwelling effect (e.g., Clemens and Prell, 2003; Fang et al., 2018a).

Within the continental shelf, the variations in the Cd/Mo ratios and Co × Mn values reflect the formation process of the upwelling system during the Roadian stage (Fig. 7d). There was a clear evolution from the restricted conditions of the Roadian-I stage to the upwelling setting of the Roadian-II/III stages. Moreover, the increasing Ba/Ti ratios reflect

the increased nutrient supply with intensified upwelling. In contrast, the Ba/Ti ratio, the Cd/Mo ratio, and the Co × Mn value within the carbonate platform appear to undergo insignificant changes over time (Fig. 7d). However, due to local reservoir effect of Mo (Lei et al., 2024b), the Cd/Mo ratios of LMAs should be lower, indicating a more restricted condition (Fig. 7d). According to our previous study (Lei et al., 2024b), the carbonate platform resides within a seasonal upwelling to a semi-restricted environment. Regardless of the upwelling intensity, the water exchange between the carbonate platform and the deep-water region increases nutrients and paleoproductivity, which can be manifested in this upwelling model.

5.3. Control factors of carbon isotopes during the development of the mid-Permian (Roadian) upwelling systems

The onset of the Roadian stage is characterized by a notable positive excursion in organic or carbonate carbon isotopes (Fig. 2). On the continental shelf, the $\delta^{13}\text{C}_{\text{org}}$ values reached a relatively high level at the Roadian-I stage, experienced a minor negative shift and subsequent rebound at the Roadian-II stage, and fluctuated within a low level at the Roadian-III stage. However, the carbonate platform did not exhibit apparent variations in carbonate carbon isotopes during the Roadian stage.

Organic and carbonate carbon isotopes could be associated with silicon/carbonate deposition, continental weathering intensity, upwelling intensity, redox condition, and paleoproductivity due to similar combinations of fluctuation cycles in time series analysis and correlations in wavelet coherence analysis (Figs. 4 and 5). However, Roadian-II correlations between TS and Fe_{py} contents and organic carbon isotopes on the continental shelf (Fig. 8a), as well as an opposite relationship between carbonate carbon isotopes and various proxies during the former and latter Roadian stage in the carbonate platform (Fig. 8b), indicate a varying control mechanism on the carbon isotopes during different phases of upwelling development in different sedimentary

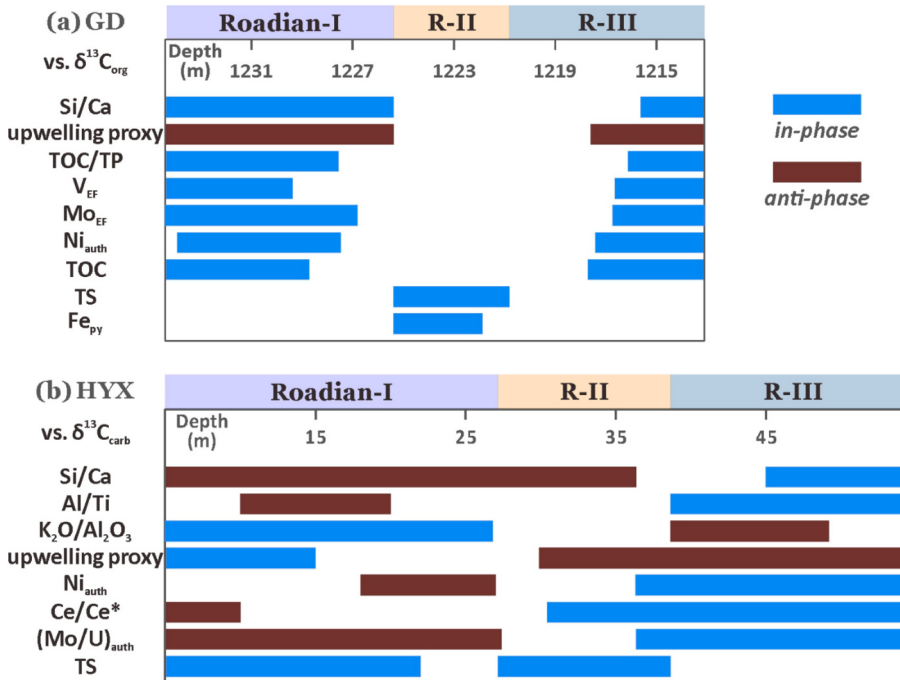


Fig. 8. (a) Relationships among silicon/carbonate deposition, upwelling intensity (the processed $(\text{Co} \times \text{Mn}) \times (\text{Cd}/\text{Mo})^{-1}$ value; Section 3.2), redox conditions, paleoproductivity, and sulfate reduction within the continental shelf across the three phases of the Roadian stage. (b) Relationships among silicon/carbonate deposition, weathering intensity, upwelling intensity (the processed $(\text{Co} \times \text{Mn}) \times (\text{Cd}/\text{Mo})^{-1}$ value; Section 3.2), paleoproductivity, redox conditions, and possibly sulfate reduction within the carbonate platform across the three phases of the Roadian stage. Correlations were obtained from wavelet analyses in the supplementary material.

environments.

5.3.1. Positive $\delta^{13}\text{C}$ excursion across the Roadian/Kungurian boundary

Across the Roadian/Kungurian boundary, the positive $\delta^{13}\text{C}$ plateau is a global phenomenon, but its timing may vary slightly with latitude (Buggisch et al., 2011; Lu et al., 2021; Sun et al., 2023; Zhang et al., 2020a). During the Guadalupian Epoch, the onset of the LPIA P3 glacial episode (Fielding et al., 2023) lowered the global temperature (Sun et al., 2023; Vérard and Veizer, 2019) (Fig. 9). The relatively weak volcanic activity (Huang et al., 2022) did not only decrease the release of ^{12}C -enriched CO_2 , which diminished the ^{12}C in the ocean and atmosphere carbon cycles (Cao et al., 2022; Shen et al., 2022), but also reduced emissions of volcanic volatiles, alleviating acid rain and soil acidification and promoting the re-expansion of tropical rainforests (Bond et al., 2010a; Cleal and Thomas, 2005) (Fig. 9). Consequently, the declined temperature, the cessation of volcanism, and the reduction of exposed bedrock resulted in the Kungurian/Roadian boundary exhibiting the lowest level of $^{87}\text{Sr}/^{86}\text{Sr}_{\text{sw}}$ and atmospheric pCO_2 within the Permian (Cao et al., 2022; Foster et al., 2017; Witkowski et al., 2018) (Fig. 9), which likely contributed to the significant positive shift in the carbon isotope value (Sun et al., 2023).

On the other hand, thermohaline circulation and upwelling led to the cooling and eutrophication of surface seawater (Beauchamp and Grasby, 2012; Zhang et al., 2023a; Zhang et al., 2022a), which, together with reduced continental runoff, weakened surface ocean stratification (Meyers, 2014). Therefore, primary productivity and the burial of organic carbon were promoted, which weakened the recycling of ^{13}C -depleted organic matter in the photic zone (Frank et al., 2008; Schrag

et al., 2013; Wang et al., 2023), leading to a further positive shift in carbon isotopes.

5.3.2. Alternative silicon and carbonate depositions: Potential indicators for paleoclimate

During the PCE, there is a transition from radiolarian chert rhythmites in distal deep water to authigenic siliceous-rich LMAs in proximal shallow water during the Guadalupian in South China (e.g., Cai et al., 2019; Gao et al., 2020a; Lei et al., 2022; Zhang et al., 2023a). A mixing model of Y/Ho vs. Eu/Eu* that is established via mass balance calculations can be used to evaluate the relative proportions of modern seawater, freshwater, and hydrothermal fluid in the precipitation fluids of silica-rich deposits and chert (Fig. 10) (Delvigne et al., 2012; Gao et al., 2020a). For LMAs, only samples with more than 10 % siliceous components (quartz and clay minerals) are selected. This model shows that Si within LMAs mainly originates from seawater and that the amount of riverine Si is less than 10 %. However, the contribution of detrital Si can reach over 10 % in the GD section. Here, we use the Si/Ca ratio to describe alternations in silicon/carbonate deposition.

5.3.2.1. Lower Yangtze shelf margin. On the continental shelf, developing upwelling systems enhanced primary productivity, as evidenced by the significant increase in the Ni_{auth} values and TOC contents from the Roadian-I to Roadian-II/III stages (Fig. 4). Correlation between the Si/Ca ratios and TOC contents (Fig. 11a) indicates that enhanced productivity led to organic matter enrichment and facilitated biological silicon secretion of radiolarians (e.g., Kametaka et al., 2005; Zhang

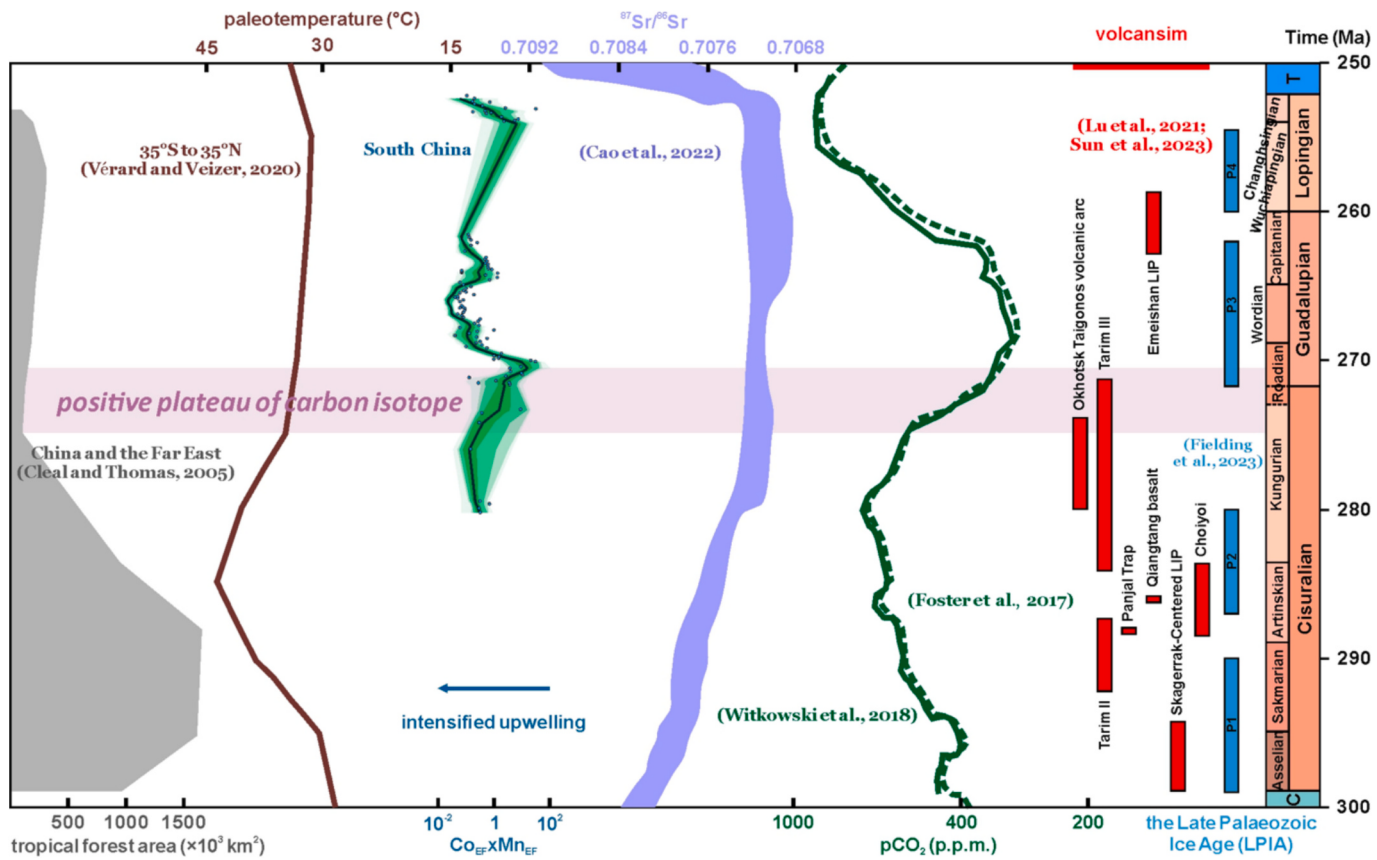


Fig. 9. Variation in tropical forest areas in China and the Far East (Cleal and Thomas, 2005) and the paleotemperature variation in the paleoequator region (Vérard and Veizer, 2019) during the Permian. The variation in upwelling intensity in the Lower Yangtze region of South China during the Permian was fitted by upwelling proxies ($\text{Co}_{\text{EF}} \times \text{Mn}_{\text{EF}}$ values; Sweere et al., 2016) (data from Wu siman et al., 2017; Yu et al., 2021). The ages of samples are calculated based on the time scale from Shen et al. (2020) and Shen et al. (2021). $^{87}\text{Sr}/^{86}\text{Sr}$ variations (Cao et al., 2022) and pCO_2 levels (solid and dotted lines: Foster et al., 2017; Witkowski et al., 2018) during the Permian. The span of large-scale volcanism during the Permian (modified from Lu et al., 2021; Sun et al., 2023). The P1 to P4 glacial episode of the late Paleozoic ice age (LPIA) (Fielding et al., 2023).

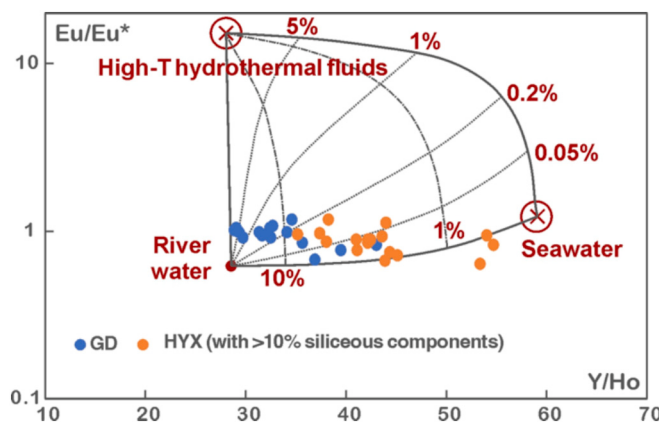


Fig. 10. Y/Ho vs. Eu/Eu* model (modified from Delvigne et al., 2012; Gao et al., 2020a). For LMAs, only samples with more than 10 % siliceous components (quartz and clay minerals) were analyzed. The three endmember sources include seawater (modern ocean seawater, open ocean, and Japanese seamount-type limestones; Alibo and Nozaki, 1999; Tanaka and Kawabe, 2006; Van Kranendonk et al., 2003), hydrothermal fluids (Bau and Dulski, 1999; Douville et al., 1999), and river water (Soyol-Erdene and Huh, 2013).

et al., 2018). In addition, the proxies of continental weathering and paleoclimate correlate with the Si/Ca ratios (Fig. 11b and c). At the Roadian-I/Roadian-II boundary, continental weathering significantly intensified with paleoclimate becoming warmer and more humid (Fig. 7b and c), which can increase the influx of detrital silicon. Therefore, the Si/Ca ratio enhancement indicates intensifications of both paleoproductivity and continental weathering; i.e., the progressive siliceous deposition was controlled by upwelling and paleoclimate. This confirms the previous speculation that the silica of mudstone and chert was of mixed marine and detrital origins in the Lower Yangtze region (Fig. 10). Furthermore, the negative correlation between the TOC content and the Sr/Cu ratio (Fig. 11d) likely supports the opinion that the increasing supply of terrigenous nutrients from the intensified continental weathering benefited productivity enhancement (Zhang et al., 2023a).

5.3.2.2. Yangtze Carbonate Platform. During the P3 glaciation, the glacial-interglacial periods controlled the relative sea level in the YCP (Lei et al., 2024a; Wei et al., 2023). Intensified continental weathering and high sea levels always occurred during interglaciation characterized by a warm and humid climate. In the YCP, the Ni_{auth} value, Ga/Rb ratio, and Al/Ti (K₂O/Al₂O₃) ratio fluctuate conformably (Fig. 11e~h). The Ni_{auth} value is in-phase correlated with the Ga/Rb ratio and Al/Ti ratio throughout the Roadian stage and anti-phase correlated with the K₂O/Al₂O₃ ratio during the Roadian-I/II stage (Fig. 11j~l). This indicates that increasing influxes of nutrient-rich upwelling and/or terrigenous nutrients can be introduced into the carbonate platform due to the rising sea level and intensified weathering during the interglaciation, resulting in intra-platform paleoproductivity enhancement.

The Si/Ca ratio shows consistent fluctuations with the Ni_{auth} value and Ga/Rb ratio (Fig. 11g~i). The series of three proxies can detect ~210-kyr and ~180-kyr cycles (Fig. 5). At the time scales of short eccentricity (~210 kyr, 123 kyr, and 95 kyr), the Ni_{auth} value and Ga/Rb ratio maintain in-phase relationships with the Si/Ca ratio throughout the Roadian stage (Fig. 11m and n). Therefore, increased paleoproductivity during the interglaciation facilitated silica secretion of radiolarians, promoting the silica deposition of biogenic and marine origins (Lei et al., 2024a). In addition, the strong correlations between the continental weathering proxies (the Al/Ti and K₂O/Al₂O₃ ratios) and the Si/Ca ratio (Fig. 11o and p) likely indicate that intensified continental weathering contributed to the increasing influx of detrital silica in the YCP, supporting the mixing Si origins interfered by the model of

Y/Ho vs. Eu/Eu* (Fig. 10).

Therefore, siliceous deposition was favored (indicated by the increased Si/Ca ratios) on both the continental shelf and carbonate platform during the intensification of continental weathering with warm and humid climates. On the one hand, weathering intensification increased terrigenous nutrient and siliceous influxes and facilitated detrital/biological siliceous depositions in the shallow marine; on the other hand, rising sea levels due to the melting of ice sheets introduced more upwelling into the carbonate platform and facilitated biological and marine siliceous deposition.

5.3.3. Control mode of carbon isotopes in the continental shelf (the lower Yangtze shelf margin)

5.3.3.1. Roadian-I stage: paleoclimate/upwelling-driven carbon isotope value. During the Roadian-I stage, the paleoclimatic conditions and upwelling effect jointly controlled organic carbon isotope values (Figs. 9a and 13a). Under a relatively warm and humid climate (not a hot-humid climate), continental weathering intensified and increased terrigenous nutrient fluxes. Both periodic enhancements in weathering and upwelling stimulated paleoproductivity, which led to high oxygen consumption and declined oxygen concentration (Fig. 8a). Consequently, the burial of organic carbon was enhanced, leading to a positive shift in the organic carbon isotope value (Fig. 8a and 13a). Conversely, abating weathering under cooler and drier conditions and weakening upwelling led to a negative shift in carbon isotope values (Fig. 13a).

5.3.3.2. Roadian-II stage: sulfur and carbon cycling. During the Roadian-II stage, paleoclimate and upwelling no longer controlled the organic carbon isotope value (Fig. 8a). Simultaneously, this phase displays low levels of TS and Fe_{py} (Fig. 12a), accompanied by a decrease in siderite and pyrite depositions (Fig. 12b). The TS and Fe_{py} contents exhibit correlations with the organic carbon isotope value during this phase, with both maintaining coordinated variations with the carbon isotope value (Fig. 8a). Moreover, the TS and Fe_{py} content series reveal cycle assemblages similar to those of the carbon isotope series (Fig. 4). These findings may suggest that sulfate reduction reactions are the dominant factor of the organic carbon isotope value during the Roadian-II stage.

Considering the precipitation amount of siderite and pyrite (Fig. 12b), sulfate reduction reactions were likely consistently active throughout the Roadian stage. The Roadian-II stage corresponds to the intensification of the upwelling system within the shelf. During the late Roadian-I and Roadian-II stages, the P/Al ratios briefly increase (Fig. 12c). Moreover, the Ca and P contents in the late Roadian-I stage to the Roadian-III stage of the GD section have a positive correlation ($R^2 = 0.6522$; Fig. 12d). Therefore, more efficient trapping of reactive P as authigenic phases (e.g., fluorapatite) during diagenesis occurred from the late Roadian-I stage to the Roadian-II stage (Zhang et al., 2023b). Such changes in P cycling may have been driven by the particularly enhanced development of euxinia (Zhang et al., 2023b), i.e., the rapid expansion of the OMZ during the Roadian-II stage, which commonly lowers water column sulfate concentrations, enabling more phosphate to be trapped in the sediment as authigenic phases (Fig. 12c) (Xiong et al., 2019; Zhang et al., 2023b). Under conditions of low-intensity sulfate reduction, whether through the anaerobic oxidation of methane (AOM, $\text{CH}_4 + \text{SO}_4^{2-} \leftrightarrow \text{HS}^- + \text{HCO}_3^- + \text{H}_2\text{O}$) or the organoclastic sulfate reduction (OSR, $2\text{CH}_2\text{O} + \text{SO}_4^{2-} \rightarrow \text{H}_2\text{S} + \text{HCO}_3^-$), the production of HS⁻ (or H₂S) and HCO₃⁻ diminishes, resulting in deficiencies in the Fe_{py} content and the precipitation of siderite and pyrite ($\text{Fe}^{2+} + \text{HS}^- \rightarrow \text{FeS}, \text{FeS} + \text{H}_2\text{S} \rightarrow \text{FeS}_2 + \text{H}_2$; $\text{Fe}^{2+} + 2\text{HCO}_3^- \rightarrow \text{FeCO}_3 + \text{CO}_2 + \text{H}_2\text{O}$).

In nearshore sediments, sulfate reduction is responsible for a 62 % ± 17 % contribution to organic matter mineralization (Thamdrup, 2000). It is currently understood that the content and activity of organic carbon determine the pathways of SO₄²⁻ consumption in sediments (Reeburgh, 1976). When highly active organic matter, such as marine organic

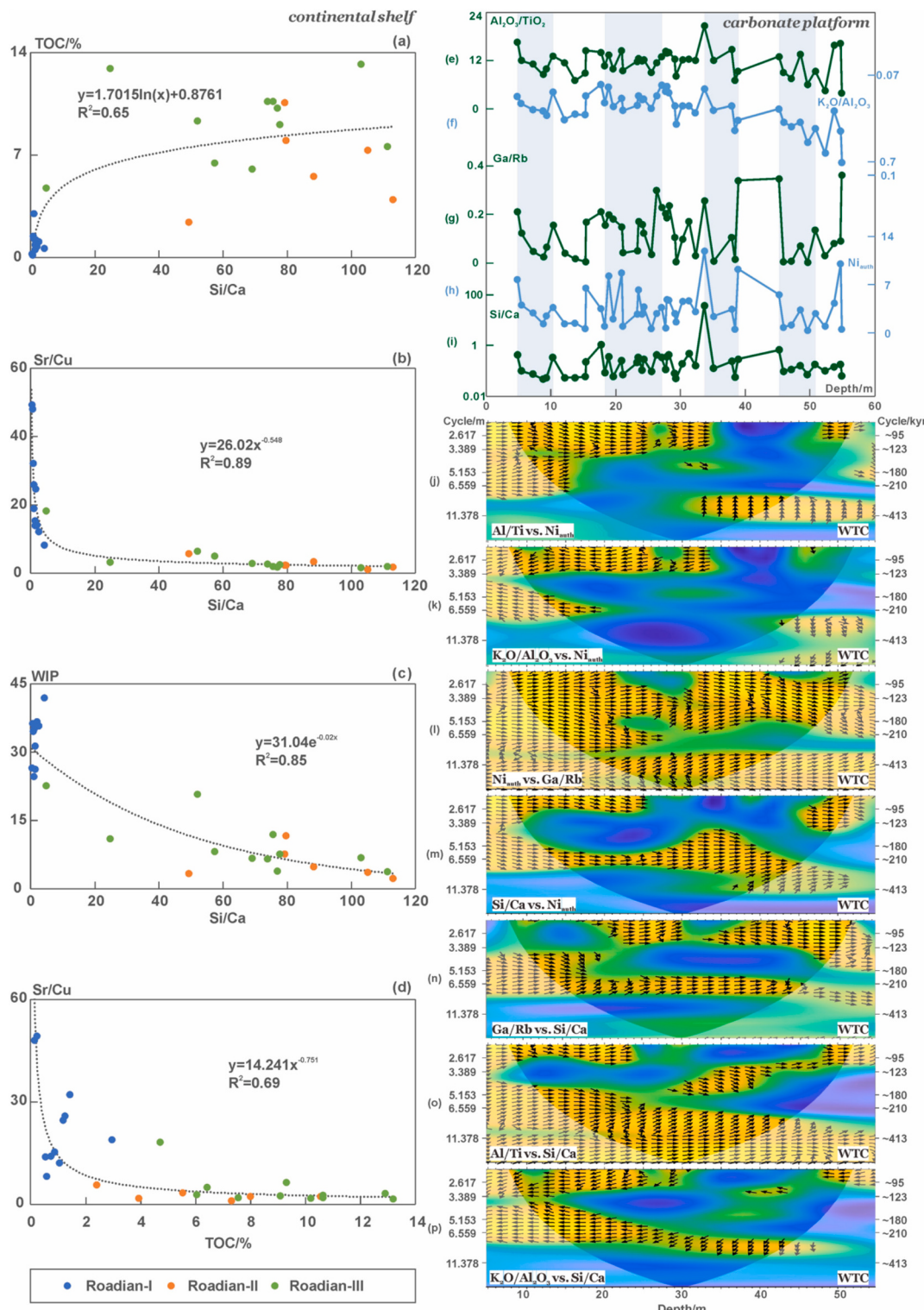


Fig. 11. Continental shelf (GD section): (a) TOC contents are covariant with Si/Ca ratios. (b) Sr/Cu ratios are contravariant with Si/Ca ratios. (c) WIP values are contravariant with Si/Ca ratios. (d) Sr/Cu ratios are contravariant with TOC contents. Carbonate platform (HYX section): (e ~ i) Trends of $\text{Al}_2\text{O}_3/\text{TiO}_2$ ratios, $\text{K}_2\text{O}/\text{Al}_2\text{O}_3$ ratios, Ga/Rb ratios, Ni_{auth} values, and Si/Ca ratios. (j ~ m) The WTC and XWT plots of Ni_{auth} values vs. Al/Ti , $\text{K}_2\text{O}/\text{Al}_2\text{O}_3$, Ga/Rb , and Si/Ca ratios. (n ~ p) The WTC and XWT plots of Si/Ca ratios vs. Ga/Rb , Al/Ti , and $\text{K}_2\text{O}/\text{Al}_2\text{O}_3$ ratios.

matter, is deposited, SO_4^{2-} is preferentially consumed through OSR. Conversely, when organic matter consists of old, refractory substances, it can be preserved due to the limitation of active organic matter that supplies to OSR, which triggers methanogenesis and leads to an enhancement of AOM (Devol et al., 1984; Wu et al., 2013).

The Roadian stratum within South China is predominantly composed of marine organic matter (the member 1 is predominantly type II₁ kerogen; Lei et al., 2024b; Section 5.1). During the middle Permian, the sulfate reduction reaction within the upwelling-derived OMZ is more likely dominated by OSR, with AOM playing a supporting role. The $\delta^{13}\text{C}$

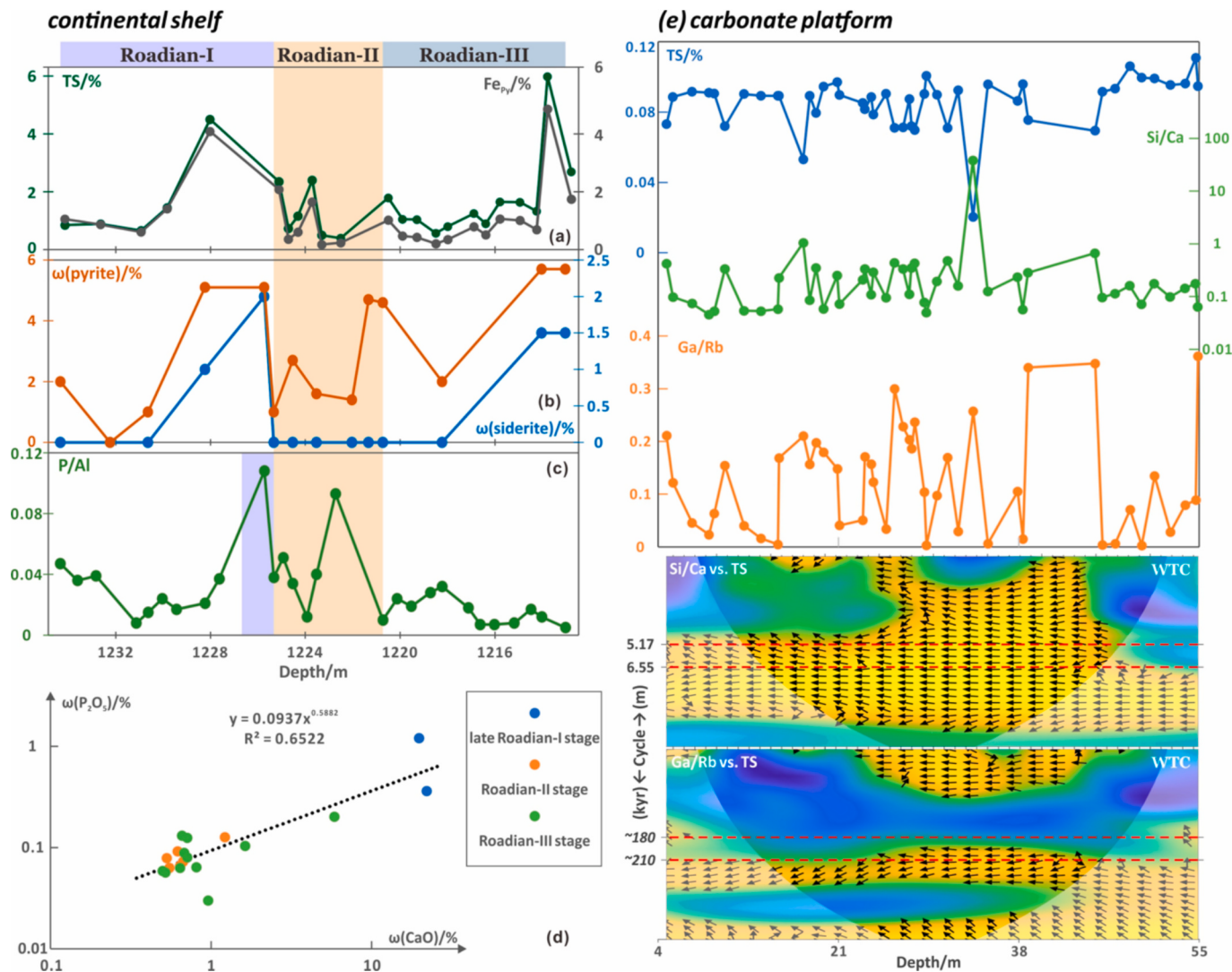


Fig. 12. (a) The contents of TS and Fe_{py} within the Roadian rhythmites on the continental shelf (GD section). (b) Pyrite and siderite contents within the Roadian rhythmites on the continental shelf (GD section; data from Zhang et al., 2022a). (c) Trend of the P/Al ratios within the Roadian rhythmites of the GD section (data from Zhang et al., 2022a). (d) Crossplot of the CaO contents vs. P₂O₅ contents of the GD section from the late Roadian-I stage to the Roadian-III stage (data from Zhang et al., 2022a). (e) TS contents are contravariant with the Ga/Rb and Si/Ca ratios in the carbonate platform (HYX section). WTC plots of the Si/Ca ratios vs. TS contents and Ga/Rb ratios vs. TS contents, the antiphase relationships nearly run through the time scales of ~210 kyr and ~180 kyr.

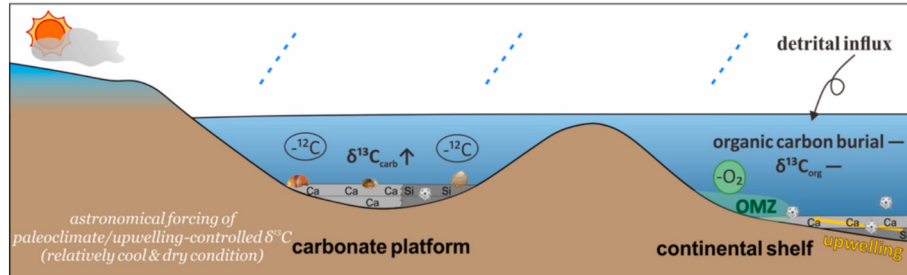
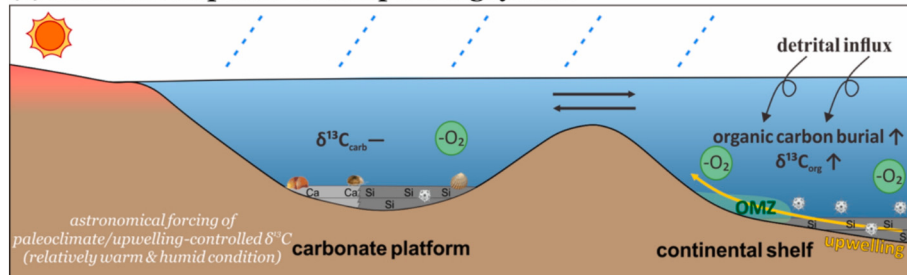
of dissolved inorganic carbon (DIC) produced via OSR is nearly identical to that of in situ TOC, whereas the $\delta^{13}\text{C}$ of AOM-derived DIC is significantly lower (Fernandes et al., 2018). Furthermore, through reaction kinetic studies, Holler et al. (2011) used ^{14}C and ^{35}S isotope labeling to reveal that AOM is a reversible reaction. During the Roadian-II stage, which is characterized by low sulfate concentrations, there is an enhancement of the reverse AOM reaction (Yoshinaga et al., 2014). The carbon isotopes of DIC in organic matter-rich, anoxic marine sediments depend on the mixing of DIC produced via the OSR and AOM pathways (Fernandes et al., 2018; Holler et al., 2011; Komada et al., 2016). This enhancement of the reverse AOM reaction results in the backflux of isotopically light carbon, leading to ^{13}C depletion of the methane pool (Yoshinaga et al., 2014) (Fig. 13b). Therefore, the reduced sulfate concentrations are accompanied by a negative shift in the carbon isotope value during this phase.

The onset of the Roadian-II stage corresponds to the transformation from mudstone to chert-mudstone alternations, which was aged at 270.6 \pm 1.8 Ma in the Pingdingshan section (Zhang et al., 2023b). Since the Roadian/Wordian boundary was aged at 268.8 Ma (Chaohu region; Yao et al., 2015), the depositional duration of chert-mudstone alternations is

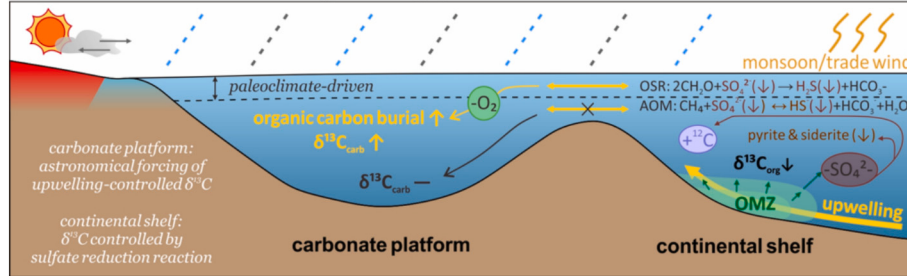
speculated to be approximately 1.8 Ma, with an average sedimentation rate of 0.661 cm/kyr. Therefore, the rapid expansion of the upwelling system (i.e., the Roadian-II stage) took approximately 0.6 Ma.

5.3.3.3. Roadian-III stage: upwelling-driven carbon isotope value. The Roadian-III stage maintained the warm and humid paleoclimate and high weathering intensity of the Roadian-II stage (Fig. 7b and c). During this phase, the upwelling system has completely developed; therefore, the upwelling intensity was at a high and stable level (Fig. 7d). The full formation of the OMZ supported stable anoxic-euxinic conditions within the upwelling systems (Fig. 7a). Compared to the Roadian-I stage, although the carbon isotopes have the same control factors, the impact of paleoclimates on the carbon isotopes has been significantly weakened (Fig. 8a). Instead, the upwelling intensity, redox conditions, and paleoproductivity are the predominant factors over the organic carbon isotope value (Fig. 8a). Periodic intensification of upwelling boosted paleoproductivity, further aggravating the oxygen depletion of continental marginal seawater. Therefore, the organic carbon burial was facilitated, which ultimately led to a periodic positive shift in the organic carbon isotope value (Fig. 13c). Additionally, periodic

(a) Initial development of the upwelling system



(b) Intensification of the upwelling system



(c) Complete development of the upwelling system

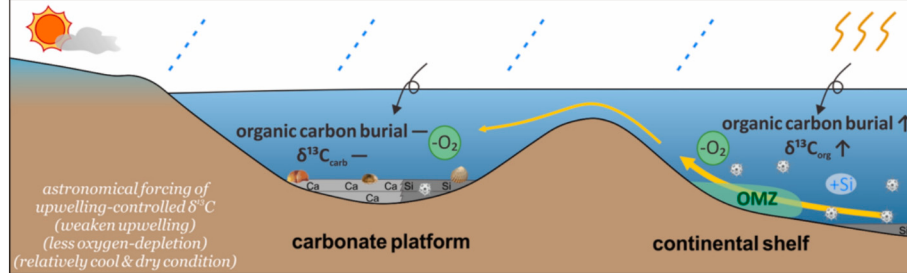
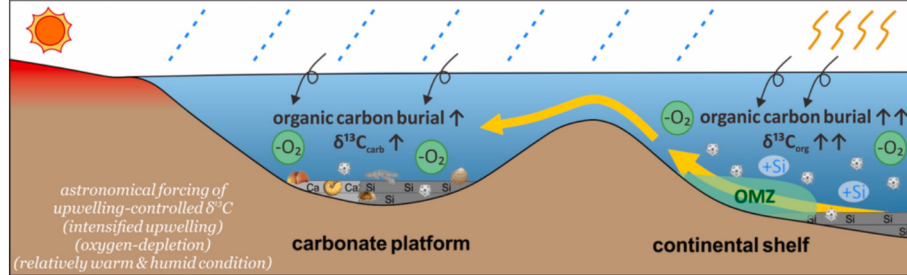


Fig. 13. Evolution of carbon isotope control factors in shallow marine environments during the development of the mid-Permian upwelling system. (a) Roadian-I stage: paleoclimate/upwelling-driven carbon isotope value. (b) Roadian-II stage: sulfate reduction reaction-driven carbon isotope value on the continental shelf; weakened paleoclimate-driven and enhanced upwelling-driven carbon isotope value in the carbonate platform. (c) Roadian-III stage: upwelling-driven carbon isotope value.

weathering enhancements affected paleoproductivity, redox conditions, and organic carbon isotopes by supplying terrigenous nutrients (Fig. 13c).

5.3.3.4. Whether the control mode has universal significance for the Panthalassa. In the middle Permian, the shallow Panthalassa, such as the Tieqiao and Penglaitan sections, experienced anoxic/euxinic conditions

associated with the upwelling development and the OMZ, despite its OMZ being significantly narrower than that in the shallow Tethys (Fujisaki et al., 2019). Given the similar paleoclimate and paleoenvironment conditions to the shallow Tethys (Meng et al., 2022), the shallow Panthalassa likely exhibited a resembling control mode.

Moreover, during the global cooling episode, ocean circulation in Panthalassa was likely more intense than in Tethys (Fujisaki et al., 2019), and the mid-Panthalassan realm with a depth over 4000 m remained out of the range of upwelling systems. In addition, seawater exchange between Panthalassa and Tethys was restricted to paleo-equatorial regions. Consequently, anoxic seawater from shallow layers and the Tethys was prevented from entering the mid-Panthalassa, resulting in intermittent suboxic conditions that never reached an anoxic condition during the Guadalupian (Fujisaki et al., 2019). In the Gujo-Hachiman section, the organic carbon isotopic value is anti-correlated with the $\text{Co}_{\text{EF}} \times \text{Mn}_{\text{EF}}$ value throughout the Guadalupian Epoch (Fig. 14b), which possibly means that deeper oceanic water masses (the precursor to upwelling) controlled the organic carbon isotope in the mid-Panthalassa (Sweere et al., 2016) when the region was persistently influenced by them (Fig. 14a). However, as a reliable paleoredox proxy in Gujo-Hachiman, the U_{EF} values lack lasting correlation with the carbon isotopes (Fig. 14c). In addition, the TOC contents exhibit an anti-correlation with the isotopes (Fig. 14d). This possibly indicates that due to a more oxygen-rich environment, the control mode in the mid-Panthalassa differs from that in the continental margin of South China (the Roadian-III stage), where upwelling promoted organic matter burial and led to a positive shift in the organic carbon isotopes by enhancing paleoproductivity. Therefore, the mechanisms controlling carbon isotopes in deep marine regions (e.g., mid-Panthalassa) under potential upwelling influence require further investigation.

5.3.4. Control mode of carbon isotopes in the carbonate platform (the Yangtze Carbonate Platform)

5.3.4.1. Roadian-I stage: paleoclimate-driven carbon isotope value. The Roadian-I stage corresponds to the initial stage of upwelling system development on the continental shelf. In the carbonate platform, the dominance of upwelling on inorganic carbon isotope values was significantly less than that of astronomical-forced paleoclimate

conditions (Fig. 8b). Moreover, the Roadian-I stage was the onset of the P3 glaciation (Fielding et al., 2023). During the glacial periods (the phases with relatively cool-dry climates and weakened continental weathering), the sea levels within the carbonate platform were relatively low due to relatively high global glacier volumes (Lei et al., 2024a; Wei et al., 2023). Therefore, water exchange in shallow marine was reduced, lowering the nutrient-rich seawater supply from the continental shelf and decreasing inner-platform paleoproductivity and oxygen consumption (Fig. 8b and 11j~l). However, owing to the limited intensity and impact scope of the upwelling systems, the insufficient nutrient supply did not impact carbon isotopes significantly like on the simultaneous continental shelf (Fig. 8b). Instead, a decline in sea level led to reduced water exchange, resulting in a ^{12}C depletion in surface water and a positive $\delta^{13}\text{C}_{\text{carb}}$ shift (Fig. 13a) (Yoshinaga et al., 2014). Vice versa, a negative $\delta^{13}\text{C}_{\text{carb}}$ shift occurred under a warm and humid climate with intensified continental weathering (the interglacial periods) (Wang et al., 2023) (Fig. 13a).

5.3.4.2. Roadian-II stage: enhanced upwelling-driven carbon isotope value. The Roadian-II stage corresponds to the intensification of the upwelling system on the continental shelf. Owing to upwelling intensification, the impact of upwelling has notably surpassed paleoclimates (Fig. 8b).

Like the Roadian-II stage on the shelf, the TS content exhibited an in-phase relationship with the carbon isotope value (Fig. 8b). But this correlation has been evident since the Roadian-I stage in the carbonate platform (Fig. 8b). The carbonate platform was predominantly under oxic-suboxic conditions during the Roadian stage (Fig. 7a) and thus unlikely to undergo sulfate reduction reactions. Moreover, the TS content and paleoclimatic proxies (the Si/Ca and Ga/Rb ratios) demonstrated strong negative correlations throughout the Roadian stage (Fig. 12e). Hence, the TS contents indicate paleoclimate conditions and sulfate reduction reactions did not control the $\delta^{13}\text{C}_{\text{carb}}$ of the carbonate platform during the Roadian-II stage.

In the wavelet analysis of carbon isotopes, the $\delta^{13}\text{C}_{\text{carb}}$ values anti-phased correlated with the Si/Ca ratios and in-phased correlated with the Ni_{auth} values (Fig. 8b). However, this is contradictory to the strong in-phased correlation between the Si/Ca ratios and Ni_{auth} values (Fig. 12m). Considering the depositional mechanism of siliceous

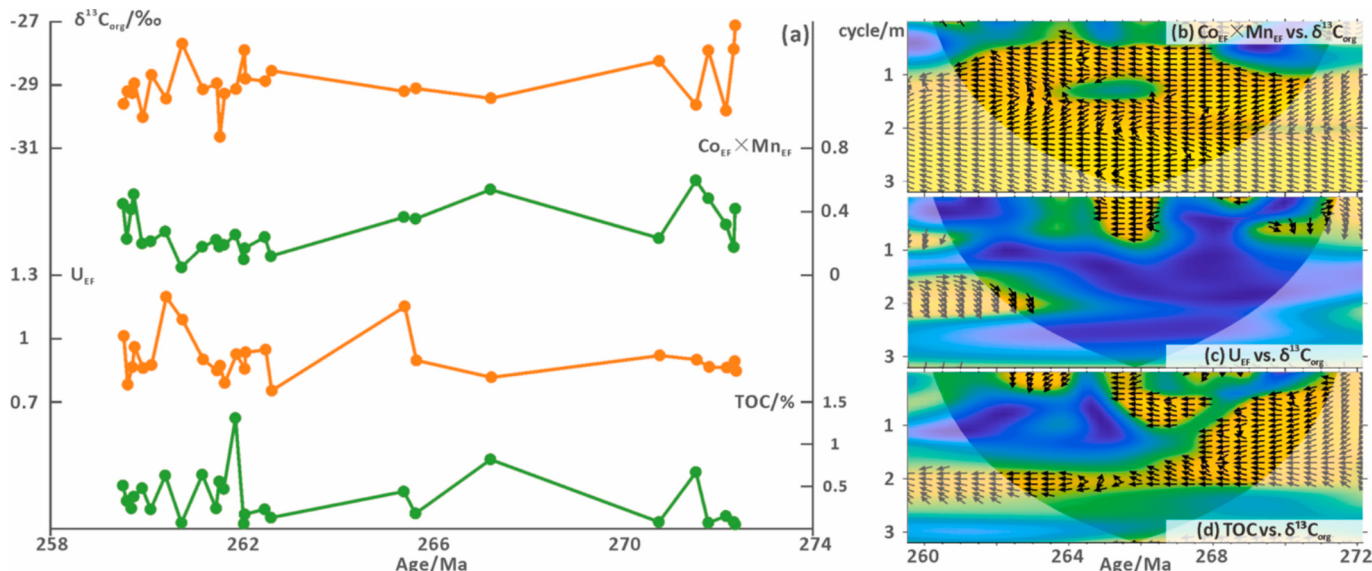


Fig. 14. (a) The trends of the $\delta^{13}\text{C}_{\text{org}}$, $\text{Co}_{\text{EF}} \times \text{Mn}_{\text{EF}}$, U_{EF} , and TOC values in the Gujo-Hachiman section during the Guadalupian Epoch. Data were referred to Fujisaki et al. (2019). The ages of the samples were calculated based on the Cisuralian/Guadalupian boundary of 273.01 ± 0.14 Ma, the Guadalupian/Lopingian boundary of 259.51 ± 0.21 Ma, and the Wordian/Capitanian boundary of 264.28 ± 0.16 Ma (Shen et al., 2021; Shen et al., 2020). (b) WTC plot of the $\text{Co}_{\text{EF}} \times \text{Mn}_{\text{EF}}$ values vs. the organic carbon isotopes. (c) WTC plot of the U_{EF} values vs. the organic carbon isotopes. (d) WTC plot of the TOC contents vs. the organic carbon isotopes.

components (Section 5.3.2; Lei et al., 2024a; Zhang et al., 2023a), we do not think that the anti-phased correlation between the $\delta^{13}\text{C}_{\text{carb}}$ values and Si/Ca ratios can accurately reflect the impact of paleoclimate on carbon isotopes during this phase.

During the middle and late Roadian-II stage, the carbon isotope values correlate with the proxies regarding the upwelling effect, redox conditions, and paleoproductivity (Fig. 8b). These correlations are opposite to those in the Roadian-I stage, indicating that gradually intensified upwelling enhanced paleoproductivity, and oxygen consumption. Therefore, intensified upwelling contributed to the burial of organic carbon and a positive $\delta^{13}\text{C}_{\text{carb}}$ shift (Fig. 13b).

5.3.4.3. Roadian-III stage: upwelling-driven carbon isotope value. During the Roadian-III stage, with the complete development of the upwelling system on the continental shelf, the composition of the inorganic carbon isotope value in the carbonate platform was controlled by both the upwelling intensity and redox conditions (Fig. 8b). Like the Roadian-I/III stages of the continental shelf, during the interglacial periods with relatively warm-humid climates and diminished ice volume, rising sea levels heightened upwelling flux into the carbonate platform (Fig. 13c), increasing marine nutrient influx. Furthermore, intensified continental weathering introduced increasing terrigenous nutrients. Therefore, enhanced paleoproductivity resulted in the oxygen depletion of bottom water, leading to an increase in the burial of organic carbon and a positive shift in $\delta^{13}\text{C}_{\text{carb}}$ (Fig. 13c).

6. Conclusion

During the middle Permian, astronomically forced upwelling systems were widely distributed across the continental shelves and slopes along the western coast of Pangea and the paleoequator. In South China, from the early to middle-late Roadian stages, the continental shelf experienced a warmer and more humid climate, leading to intensified continental weathering, accompanied by the development of an upwelling system and noticeable oxygen depletion. In contrast, the adjacent carbonate platform was incidentally impacted by the upwelling system. However, the development of the upwelling system did not induce significant paleoenvironmental changes, resulting in only a slight decrease in chemical weathering intensity.

During the initial development of the upwelling system, the carbon isotope value in shallow marine environments was primarily controlled by periodically fluctuating paleoclimatic conditions (and upwelling effects). In relatively warm and humid climates, intensified continental weathering and upwelling increased nutrient influx, stimulating paleoproductivity and oxygen depletion on the continental shelf. Enhancement in organic carbon burial led to a positive shift in organic carbon isotopes. However, weakened water exchange under relatively cool-dry climates led to depletion of ^{12}C and positive $\delta^{13}\text{C}_{\text{carb}}$ excursions in the carbonate platform.

With the intensification of the upwelling system, its influence on intra-platform carbon isotopes has surpassed paleoclimates. The influx of upwelling enhanced paleoproductivity and oxygen consumption, contributing to the organic carbon burial and a positive $\delta^{13}\text{C}_{\text{carb}}$ shift. However, on the continental shelf, the rapid expansion of the OMZ led to decreased water column sulfate concentrations, highlighting the disturbance caused by sulfate reduction reactions during carbon cycling. Reduced sulfate concentrations facilitated the reverse reaction of AOM, resulting in a backflux of ^{12}C and the depletion of ^{13}C in the methane pool.

Following the complete development of the upwelling system, both the intensity of upwelling and the redox conditions became controlling factors over shallow marine carbon isotopes. On the continental shelf, the complete formation of the upwelling system and OMZ ensured further enrichment of organic matter. Periodic enhancements in upwelling and continental weathering facilitated nutrient supply and

paleoproductivity. The organic carbon isotope value exhibited periodic positive shifts with increasing oxygen depletion. Similarly, in the carbonate platform, during relatively warm-humid climates (interglaciation), the upwelling fluxes and terrigenous nutrients increased with high relative sea levels and intensified continental weathering. The heightened paleoproductivity led to oxygen depletion in the bottom water, consequently causing a positive shift in the carbonate carbon isotope value.

Whether this evolutionary model can be applied to other shallow marine environments with upwelling systems requires further verification.

CRediT authorship contribution statement

Han Lei: Writing – original draft, Visualization, Methodology, Investigation, Conceptualization. **Wenhuai Huang:** Methodology, Funding acquisition, Data curation, Conceptualization. **Qingchun Jiang:** Writing – review & editing, Resources, Funding acquisition. **Ping Luo:** Resources, Investigation, Conceptualization.

Declaration of competing interest

The authors declare that they have no known competing financial interests or personal relationships that could have appeared to influence the work reported in this paper.

Acknowledgments

This work was financially supported by China National Petroleum Corporation, CNPC (Grant No. 2023ZZ0206), PetroChina Oil & Gas and New Energy Company (Grant No. 2021DJ0203), and the National Natural Science Foundation of China (Grant No. 41972172).

Appendix A. Supplementary data

Supplementary data to this article can be found online at <https://doi.org/10.1016/j.palaeo.2025.113215>.

Data availability

Data will be made available on request.

References

- Algeo, T.J., Ingall, E., 2007. Sedimentary Corg:P ratios, paleocean ventilation, and Phanerozoic atmospheric pO₂. *Palaeogeogr. Palaeoclimatol. Palaeoecol.* 256 (3), 130–155.
- Algeo, T.J., Liu, J., 2020. A re-assessment of elemental proxies for paleoredox analysis. *Chem. Geol.* 540, 119549.
- Algeo, T.J., Lyons, T.W., 2006. Mo-total organic carbon covariation in modern anoxic marine environments: Implications for analysis of paleoredox and paleohydrographic conditions. *Paleoceanography* 21 (1).
- Algeo, T.J., Maynard, J.B., 2004. Trace-element behavior and redox facies in core shales of Upper Pennsylvanian Kansas-type cycloths. *Chem. Geol.* 206 (3), 289–318.
- Algeo, T.J., Tribouillard, N., 2009. Environmental analysis of paleoceanographic systems based on molybdenum–uranium covariation. *Chem. Geol.* 268 (3), 211–225.
- Alibo, D.S., Nozaki, Y., 1999. Rare earth elements in seawater: particle association, shale-normalization, and Ce oxidation. *Geochim. Cosmochim. Acta* 63 (3), 363–372.
- Anderson, T.F., Arthur, M.A., 1983. Stable Isotopes of Oxygen and Carbon and their Application to Sedimentologic and Paleoenvironmental Problems. In: Arthur, M.A., Anderson, T.F., Kaplan, I.R., Veizer, J., Land, L.S. (Editors), *Stable Isotopes in Sedimentary Geology*. SEPM Society for Sedimentary Geology, pp. 0.
- Arthur, M.A., Sageman, B.B., 1994. MARINE BLACK SHALES: Depositional Mechanisms and Environments of Ancient Deposits, 22, pp. 499–551.
- Arthur, M.A., Dean, W.E., Claypool, G.E., 1985. Anomalous ^{13}C enrichment in modern marine organic carbon. *Nature* 315 (6016), 216–218.
- Bau, M., Dulski, P., 1999. Comparing yttrium and rare earths in hydrothermal fluids from the Mid-Atlantic Ridge: implications for Y and REE behaviour during near-vent mixing and for the Y/Ho ratio of Proterozoic seawater. *Chem. Geol.* 155 (1), 77–90.
- Beauchamp, B., Baud, A., 2002. Growth and demise of Permian biogenic chert along northwest Pangea: evidence for end-Permian collapse of thermohaline circulation. *Palaeogeogr. Palaeoclimatol. Palaeoecol.* 184 (1), 37–63.

- Beauchamp, B., Grasby, S.E., 2012. Permian lysocline shoaling and ocean acidification along NW Pangea led to carbonate eradication and chert expansion. *Palaeogeogr. Palaeoclimatol. Palaeoecol.* 350–352, 73–90.
- Beckmann, B., Flögel, S., Hofmann, P., Schulz, M., Wagner, T., 2005. Orbital forcing of cretaceous river discharge in tropical Africa and ocean response. *Nature* 437 (7056), 241–244.
- Bond, D.P.G., et al., 2010a. The Middle Permian (Capitanian) mass extinction on land and in the oceans. *Earth Sci. Rev.* 102 (1), 100–116.
- Bond, D.P.G., et al., 2010b. The mid-Capitanian (Middle Permian) mass extinction and carbon isotope record of South China. *Palaeogeogr. Palaeoclimatol. Palaeoecol.* 292 (1), 282–294.
- Bonin, P., et al., 2004. Geochemistry of Peruvian near-surface sediments. *Geochim. Cosmochim. Acta* 68 (21), 4429–4451.
- Brumsack, H.-J., 2006. The trace metal content of recent organic carbon-rich sediments: Implications for cretaceous black shale formation. *Palaeogeogr. Palaeoclimatol. Palaeoecol.* 232 (2), 344–361.
- Buggisch, W., Wang, X., Alekseev, A.S., Joachimski, M.M., 2011. Carboniferous–Permian carbon isotope stratigraphy of successions from China (Yangtze platform), USA (Kansas) and Russia (Moscow Basin and Urals). *Palaeogeogr. Palaeoclimatol. Palaeoecol.* 301 (1), 18–38.
- Cai, Z., et al., 2019. Genesis of Mg-phyllosilicate occurrences in the Middle Permian marine successions of South China. *Appl. Clay Sci.* 181, 105242.
- Cao, C., et al., 2018. A positive C-isotope excursion induced by sea-level fall in the middle Capitanian of South China. *Palaeogeogr. Palaeoclimatol. Palaeoecol.* 505, 305–316.
- Cao, C., Liu, X.-M., Bataille, C.P., Liu, C., 2020. What do Ce anomalies in marine carbonates really mean? A perspective from leaching experiments. *Chem. Geol.* 532, 119413.
- Cao, C., et al., 2022. Persistent late Permian to early Triassic warmth linked to enhanced reverse weathering. *Nat. Geosci.* 15 (10), 832–838.
- Chen, J., et al., 2015. Diagenetic uptake of rare earth elements by bioapatite, with an example from lower Triassic conodonts of South China. *Earth Sci. Rev.* 149, 181–202.
- Cleal, C.J., Thomas, B.A., 2005. Palaeozoic tropical rainforests and their effect on global climates: is the past the key to the present? *Geobiology* 3 (1), 13–31.
- Clemens, S.C., Prell, W.L., 2003. A 350,000 year summer-monsoon multi-proxy stack from the Owen Ridge, Northern Arabian Sea. *Mar. Geol.* 201 (1), 35–51.
- Conway, T.M., John, S.G., 2015. Biogeochemical cycling of cadmium isotopes along a high-resolution section through the North Atlantic Ocean. *Geochim. Cosmochim. Acta* 148, 269–283.
- Dehairs, F., Stroobants, N., Goeyens, L., 1991. Suspended barite as a tracer of biological activity in the Southern Ocean. *Mar. Chem.* 35 (1), 399–410.
- Delvigne, C., Cardinal, D., Hofmann, A., André, L., 2012. Stratigraphic changes of Ge/Si, REE+Y and silicon isotopes as insights into the deposition of a Mesoarchaean banded iron formation. *Earth Planet. Sci. Lett.* 355–356, 109–118.
- Devol, A.H., Anderson, J.J., Kuiivila, K., Murray, J.W., 1984. A model for coupled sulfate reduction and methane oxidation in the sediments of Saanich Inlet. *Geochim. Cosmochim. Acta* 48 (5), 993–1004.
- Douville, E., et al., 1999. Yttrium and rare earth elements in fluids from various deep-sea hydrothermal systems. *Geochim. Cosmochim. Acta* 63 (5), 627–643.
- Dunteman, G.H., 1989. Principal Components Analysis. Sage.
- Dymond, J., Suess, E., Lyle, M., 1992. Barium in Deep-Sea Sediment: a Geochemical Proxy for Paleoproductivity. *Paleoceanography* 7 (2), 163–181.
- Eggleson, S., Schmitt, J., Bereiter, B., Schneider, R., Fischer, H., 2016. Evolution of the stable carbon isotope composition of atmospheric CO₂ over the last glacial cycle. *Paleoceanography* 31 (3), 434–452.
- Elderfield, H., 1986. Strontium isotope stratigraphy. *Palaeogeogr. Palaeoclimatol. Palaeoecol.* 57 (1), 71–90.
- Fang, Q., 2012. A Study on Conodont Fauna and its Biostratigraphy of Guadalupian and Lopingian in Northeastern of Sichuan Province. China University of Geosciences, Beijing, Beijing.
- Fang, Q., Jing, X., Deng, S., Wang, X., 2012. Roadian-Wuchiapingian Conodont Biostratigraphy at the Shangsi Section, Northern Sichuan. *J. Stratigr.* 4, 692–699.
- Fang, Q., et al., 2018a. Abiotic and biotic responses to Milankovitch-forced megamonsoon and glacial cycles recorded in South China at the end of the late Paleozoic Ice Age. *Glob. Planet. Chang.* 163, 97–108.
- Fang, Q., et al., 2018b. Astronomical cycles in the Serpukhovian-Moscovian (Carboniferous) marine sequence, South China and their implications for geochronology and icehouse dynamics. *J. Asian Earth Sci.* 156, 302–315.
- Fernandes, S., et al., 2018. Enhanced carbon-sulfur cycling in the sediments of Arabian Sea oxygen minimum zone center. *Sci. Rep.* 8 (1), 8665.
- Fielding, C.R., Frank, T.D., Birgenheier, L.P., 2023. A revised, late Palaeozoic glacial time-space framework for eastern Australia, and comparisons with other regions and events. *Earth Sci. Rev.* 236, 104263.
- Foster, G.L., Royer, D.L., Lunt, D.J., 2017. Future climate forcing potentially without precedent in the last 420 million years. *Nat. Commun.* 8 (1), 14845.
- Frank, T.D., Birgenheier, L.P., Montañez, I.P., Fielding, C.R., Rygel, M.C., 2008. Late Paleozoic climate dynamics revealed by comparison of ice-proximal stratigraphic and ice-distal isotopic records. In: Fielding, C.R., Frank, T.D., Isbell, J.L. (Eds.), *Resolving the Late Paleozoic Ice Age in Time and Space*. Geological Society of America, pp. 0.
- Friedman, I., O'Neil, J.R., 1977. Compilation of stable isotope fractionation factors of geochemical interest. 440KK.
- Fujisaki, W., et al., 2016. Tracking the redox history and nitrogen cycle in the pelagic Panthalassic deep ocean in the Middle Triassic to early Jurassic: Insights from redox-sensitive elements and nitrogen isotopes. *Palaeogeogr. Palaeoclimatol. Palaeoecol.* 449, 397–420.
- Fujisaki, W., et al., 2019. Redox condition and nitrogen cycle in the Permian deep mid-ocean: a possible contrast between Panthalassa and Tethys. *Glob. Planet. Chang.* 172, 179–199.
- Gao, P., et al., 2015. Evaluating rare earth elements as a proxy for oil-source correlation. A case study from Aker Sag, Erlian Basin, northern China. *Org. Geochem.* 87, 35–54.
- Gao, P., et al., 2020a. Mixed seawater and hydrothermal sources of nodular chert in Middle Permian limestone on the eastern Paleo-Tethys margin (South China). *Palaeogeogr. Palaeoclimatol. Palaeoecol.* 551, 109740.
- Gao, P., He, Z., Lash, G.G., Li, S., Zhang, R., 2020b. Origin of chert nodules in the Ediacaran Doushantuo Formation black shales from Yangtze Block, South China. *Mar. Petrol. Geol.* 114, 104227.
- Glenister, B.F., et al., 1999. Proposal of Guadalupian and component Roadian, Wordian, and Capitanian stages as international standards for the Middle Permian Series. *Permophiles* 34, 3–11.
- Hasegawa, T., 1997. Cenomanian-Turonian carbon isotope events recorded in terrestrial organic matter from northern Japan. *Palaeogeogr. Palaeoclimatol. Palaeoecol.* 130 (1), 251–273.
- Hayes, J.M., Strauss, H., Kaufman, A.J., 1999. The abundance of ¹³C in marine organic matter and isotopic fractionation in the global biogeochemical cycle of carbon during the past 800 Ma. *Chem. Geol.* 161 (1), 103–125.
- Holler, T., et al., 2011. Carbon and sulfur back flux during anaerobic microbial oxidation of methane and coupled sulfate reduction. *Proc. Natl. Acad. Sci.* 108 (52), E1484–E1490.
- Hou, Z., 2020. High-Resolution Quantitative Paleogeographic Study of the Permian in South China. University of Science and Technology of China.
- Huang, H., et al., 2022. Zircon U-Pb age, trace element, and Hf isotopic constrains on the origin and evolution of the Emeishan large Igneous Province. *Gondwana Res.* 105, 535–550.
- Isozaki, Y., Kawahata, H., Ota, A., 2007. A unique carbon isotope record across the Guadalupian–Lopingian (Middle–Upper Permian) boundary in mid-oceanic paleo-atoll carbonates: The high-productivity “Kamura event” and its collapse in Panthalassa. *Glob. Planet. Chang.* 55 (1), 21–38.
- Isozaki, Y., Aljinović, D., Kawahata, H., 2011. The Guadalupian (Permian) Kamura event in European Tethys. *Palaeogeogr. Palaeoclimatol. Palaeoecol.* 308 (1), 12–21.
- Jacobsen, S.B., Kaufman, A.J., 1999. The Sr, C and O isotopic evolution of Neoproterozoic seawater. *Chem. Geol.* 161 (1), 37–57.
- Jones, B., Manning, D.A.C., 1994. Comparison of geochemical indices used for the interpretation of palaeoredox conditions in ancient mudstones. *Chem. Geol.* 111 (1), 111–129.
- Kametaka, M., Takebe, M., Nagai, H., Zhu, S., Takayanagi, Y., 2005. Sedimentary environments of the Middle Permian phosphorite–chert complex from the northeastern Yangtze platform, China; the Gufeng Formation: a continental shelf radiolarian chert. *Sediment. Geol.* 174 (3), 197–222.
- Knauth, L.P., Kennedy, M.J., 2009. The late Precambrian greening of the Earth. *Nature* 460 (7256), 728–732.
- Kodama, K.P., Hinnov, L.A., 2014. Time Series Analysis for Cyclostratigraphy. *Rock Magnetic Cyclostratigr.* 52–89.
- Komada, T., et al., 2016. Organic matter cycling across the sulfate–methane transition zone of the Santa Barbara Basin, California Borderland. *Geochim. Cosmochim. Acta* 176, 259–278.
- Korte, C., Jasper, T., Kozur, H.W., Veizer, J., 2005. $\delta^{18}\text{O}$ and $\delta^{13}\text{C}$ of Permian brachiopods: a record of seawater evolution and continental glaciation. *Palaeogeogr. Palaeoclimatol. Palaeoecol.* 224 (4), 333–351.
- Kumpan, T., Kalvoda, J., Bábek, O., Holá, M., Kanický, V., 2019. Tracing paleoredox conditions across the Devonian–Carboniferous boundary event: A case study from carbonate-dominated settings of Belgium, the Czech Republic, and northern France. *Sediment. Geol.* 380, 143–157.
- Lambert, L.L., Wardlaw, B.R., Henderson, C.M., 2007. Mesogondolella and Jinogondolella (Conodonts): Multielement definition of the taxa that bracket the basal Guadalupian (Middle Permian Series) GSSP. *Palaeoworld* 16 (1), 208–221.
- Lan, Y., Huang, S., Zhou, X., Zeng, Y., Ma, Y., 2015. The recovery of diagenetic environments of limestone in Early Miocene Zhujiang Formation, Pearl River Mouth Basin. *Geol. China* (6), 1837–1850.
- Lan, Y., Huang, S., Ma, Y., Zhou, X., Wei, Z., 2016. Genesis of negative Carbon and Oxygen Isotopic Composition of Carbonate Rocks in lower Miocene Zhujiang Formation, Pearl River Mouth Basin. *Geological Review*(4), 915–928.
- Lei, H., Huang, W., Jiang, Q., Luo, P., 2022. Genesis of clay minerals and its insight for the formation of limestone marl alterations in Middle Permian of the Sichuan Basin. *J. Pet. Sci. Eng.* 218, 111014.
- Lei, H., Huang, W., Jiang, Q., Luo, P., 2024a. Siliceous Deposition in Limestone-Marl Alternations of the Yangtze Carbonate Platform during the Permian Chert Event. *Palaeogeography, Palaeoclimatology, Palaeoecology*, p. 112382.
- Lei, H., Jiang, Q., Huang, W., Luo, P., 2024b. Middle Permian astronomically forced upwelling in the Yangtze carbonate platform: Implications for organic matter preservation and benthic biomass. *Mar. Pet. Geol.* 160, 106575.
- Li, X.-H., McCulloch, M.T., 1996. Secular variation in the Nd isotopic composition of Neoproterozoic sediments from the southern margin of the Yangtze Block: evidence for a Proterozoic continental collision in southeast China. *Precambrian Res.* 76 (1), 67–76.
- Li, X., Huang, S., Huang, K., Yuan, T., Zhong, Y., 2016. Geochemical characteristics of Middle Permian Qixia Fm dolomitized marine fluids in the Sichuan Basin. *Nat. Gas Industry* B 36 (10), 35–45.

- Li, J., et al., 2018. Influence of differential diagenesis on primary depositional signals in limestone-marl alternations: an example from Middle Permian marine successions, South China. *Palaeogeogr. Palaeoclimatol. Palaeoecol.* 495, 139–151.
- Li, M., Hinnov, L., Kump, L., 2019. Acycle: Time-series analysis software for paleoclimate research and education. *Comput. Geosci.* 127, 12–22.
- Li, Y., Wang, Z., Wu, P., Meng, S., 2021. Paleoenvironment reconstruction of the upper Paleozoic in the Linxiong area, northeastern Ordos Basin, China. *AAPG Bull.* 105 (12), 2545–2574.
- Liu, S., et al., 2021. Paleoproductivity evolution in the northeastern Indian Ocean since the last glacial maximum: evidence from biogenic silica variations. *Deep-Sea Res. I Oceanogr. Res. Pap.* 175, 103591.
- Lu, J., et al., 2021. Records of organic carbon isotopic composition ($\delta^{13}\text{C}_{\text{org}}$) and volcanism linked to changes in atmospheric pCO₂ and climate during the late Paleozoic Icehouse. *Glob. Planet. Chang.* 207, 103654.
- Lv, D., et al., 2022. Records of chemical weathering and volcanism linked to paleoclimate transition during the late Paleozoic Icehouse. *Glob. Planet. Chang.* 217, 103934.
- McLennan, S.M., 2001. Relationships between the trace element composition of sedimentary rocks and upper continental crust. *Geochem. Geophys. Geosyst.* 2.
- Meng, Q., et al., 2022. Stratigraphy of the Guadalupian (Permian) siliceous deposits from Central Guizhou of South China: Regional correlations with implications for carbonate productivity during the Middle Permian biocrisis. *Earth Sci. Rev.* 228, 104011.
- Meyers, P.A., 1997. Organic geochemical proxies of paleoceanographic, paleolimnologic, and paleoclimatic processes. *Org. Geochem.* 27 (5), 213–250.
- Meyers, P.A., 2014. Why are the $\delta^{13}\text{C}_{\text{org}}$ values in Phanerozoic black shales more negative than in modern marine organic matter? *Geochem. Geophys. Geosyst.* 15 (7), 3085–3106.
- Montanez, I., Poulsen, C., 2013. The Late Paleozoic ice age: an evolving paradigm. *Annu. Rev. Earth Planet. Sci.* 41, 629–656.
- Montanez, I.P., et al., 2016. Climate, pCO₂ and terrestrial carbon cycle linkages during late Paleozoic glacial-interglacial cycles. *Nat. Geosci.* 9 (11), 824–828.
- Murchey, B.L., Jones, D.L., 1992. A mid-Permian chert event: widespread deposition of biogenic siliceous sediments in coastal, island arc and oceanic basins. *Palaeogeogr. Palaeoclimatol. Palaeoecol.* 96 (1), 161–174.
- Murray, R.W., Knowlton, C., Leinen, M., Mix, A.C., Polksky, C.H., 2000. Export production and terrigenous matter in the Central Equatorial Pacific Ocean during interglacial oxygen isotope stage 11. *Glob. Planet. Chang.* 24 (1), 59–78.
- Nesbitt, H.W., Young, G.M., 1982. Early Proterozoic climates and plate motions inferred from major element chemistry of lutites. *Nature* 299 (5885), 715–717.
- Nishikane, Y., Kaiho, K., Henderson, C.M., Takahashi, S., Suzuki, N., 2014. Guadalupian–Lopingian conodont and carbon isotope stratigraphies of a deep chert sequence in Japan. *Palaeogeogr. Palaeoclimatol. Palaeoecol.* 403, 16–29.
- Parker, A., 1970. An Index of Weathering for Silicate Rocks. *Geol. Mag.* 107 (6), 501–504.
- Peng, Y., et al., 2022. Benthic foraminifera distribution and sedimentary environmental evolution of a carbonate platform: a case study of the Guadalupian (middle Permian) in eastern Sichuan Basin. *Mar. Micropaleontol.* 170, 102079.
- Pierson, B.J., 1981. The control of cathodoluminescence in dolomite by iron and manganese. *Sedimentology* 28 (5), 601–610.
- Piper, D.Z., Calvert, S.E., 2009. A marine biogeochemical perspective on black shale deposition. *Earth Sci. Rev.* 95 (1), 63–96.
- PRC National Energy Administration, 2014. Method of Identification Microscopically the Macerals of Kerogen and Indivision the Kerogen Type by Transmitted-Light and Fluorescence. Petroleum Industry Press, Beijing, pp. 1–20.
- Reeburgh, W.S., 1976. Methane consumption in Cariaco Trench waters and sediments. *Earth Planet. Sci. Lett.* 28 (3), 337–344.
- Roy, D.K., Roser, B.P., 2013. Climatic control on the composition of Carboniferous–Permian Gondwana sediments, Khalaspir basin, Bangladesh. *Gondwana Res.* 23 (3), 1163–1171.
- Sarki Yandoka, B.M., Abdullah, W.H., Abubakar, M.B., Hakimi, M.H., Adegoke, A.K., 2015. Geochemical characterisation of early cretaceous lacustrine sediments of Bima Formation, Yola Sub-basin, Northern Benue Trough, NE Nigeria: Organic matter input, preservation, paleoenvironment and palaeoclimatic conditions. *Mar. Pet. Geol.* 61, 82–94.
- Schrag, D.P., Higgins, J.A., Macdonald, F.A., Johnston, D.T., 2013. Authigenic Carbonate and the history of the Global Carbon Cycle. *Science* 339 (6119), 540–543.
- Shao, J., Yang, S., Li, C., 2012. Chemical indices (CIA and WIP) as proxies for integrated chemical weathering in China: Inferences from analysis of fluvial sediments. *Sediment. Geol.* 265–266, 110–120.
- Shen, S.-Z., et al., 2020. Progress, problems and prospects: an overview of the Guadalupian Series of South China and North America. *Earth Sci. Rev.* 211, 103412.
- Shen, B.H., et al., 2021. Lithostratigraphic subdivision and correlation of the Permian in China. *J. Stratigr.* 45 (3), 319–339.
- Shen, J., et al., 2022. Intensified continental chemical weathering and carbon-cycle perturbations linked to volcanism during the Triassic–Jurassic transition. *Nat. Commun.* 13 (1), 299.
- Soyol-Erdene, T.-O., Huh, Y., 2013. Rare earth element cycling in the pore waters of the Bering Sea Slope (IODP Exp. 323). *Chem. Geol.* 358, 75–89.
- Stüben, D., et al., 2002. Trace elements, stable isotopes, and clay mineralogy of the Elles II K-T boundary section in Tunisia: indications for sea level fluctuations and primary productivity. *Palaeogeogr. Palaeoclimatol. Palaeoecol.* 178 (3), 321–345.
- Sun, S., et al., 2023. Continental weathering indices recorded in low-latitude carbonates unveil the P3 glacial of the late Paleozoic Ice Age. *Glob. Planet. Chang.* 220, 103994.
- Sweere, T., van den Boorn, S., Dickson, A.J., Reichart, G.-J., 2016. Definition of new trace-metal proxies for the controls on organic matter enrichment in marine sediments based on Mn, Co, Mo and Cd concentrations. *Chem. Geol.* 441, 235–245.
- Tanaka, K., Kawabe, I., 2006. REE abundances in ancient seawater inferred from marine limestone and experimental REE partition coefficients between calcite and aqueous solution. *Geochem. J.* 40, 425–435.
- Taylor, S.R., McLennan, S.M., 1985. The Continental Crust: Its Composition and Evolution. Blackwell Scientific Publications, Oxford, p. 311.
- Thamdrup, B., 2000. Bacterial Manganese and Iron Reduction in Aquatic Sediments. In: Schink, B. (Ed.), Advances in Microbial Ecology. Springer, US, Boston, MA, pp. 41–84.
- Thomson, D.J., 1982. Spectrum estimation and harmonic analysis. *Proc. IEEE* 70 (9), 1055–1096.
- Tribouillard, N., Algeo, T.J., Lyons, T., Riboulleau, A., 2006. Trace metals as paleoredox and paleoproductivity proxies: an update. *Chem. Geol.* 232 (1), 12–32.
- Tyson, R.V., 1994. Sedimentary Organic Matter: Organic Facies and Palynofacies.
- Van Kranendonk, M.J., Webb, G.E., Kamber, B.S., 2003. Geological and trace element evidence for a marine sedimentary environment of deposition and biogenicity of 3.45 Ga stromatolitic carbonates in the Pilbara Craton, and support for a reducing Archaean Ocean. *Geobiology* 1 (2), 91–108.
- Veizer, J., et al., 1999. $^{87}\text{Sr}/^{86}\text{Sr}$, $\delta^{13}\text{C}$ and $\delta^{18}\text{O}$ evolution of Phanerozoic seawater. *Chem. Geol.* 161 (1), 59–88.
- Vérand, C., Veizer, J., 2019. On plate tectonics and ocean temperatures. *Geology* 47 (9), 881–885.
- Wang, Z., 2000. Conodonts across the lower Middle Permian Boundary in South Guizhou: setting the Guadalupian Base. *Acta Micropalaeontologica Sinica* 17 (4), 422–429+ 499.
- Wang, Y., Jin, Y., 2000. Permian palaeogeographic evolution of the Jiangnan Basin, South China. *Palaeogeogr. Palaeoclimatol. Palaeoecol.* 160 (1), 35–44.
- Wang, L., et al., 2022. Origins of dolostones of the Maokou Formation in eastern Sichuan Basin: evidence from lithology, mineralogy, and geochemistry. *J. Palaeogeogr.* 24 (5), 989–1016.
- Wang, Y.-Y., et al., 2023. Carbonate lithium isotope systematics indicate cooling triggered mass extinction during the Frasnian–Famennian transition. *Glob. Planet. Chang.* 230, 104284.
- Wei, W., et al., 2020. Variations of redox conditions in the atmosphere and Yangtze Platform during the Ediacaran–Cambrian transition: Constraints from Cr isotopes and Ce anomalies. *Palaeogeogr. Palaeoclimatol. Palaeoecol.* 543, 109598.
- Wei, R., et al., 2023. Orbitally-paced coastal sedimentary records and global sea-level changes in the early Permian. *Earth Planet. Sci. Lett.* 620, 118356.
- Westphal, H., Hilgen, F., Munnecke, A., 2010. An assessment of the suitability of individual rhythmic carbonate successions for astrochronological application. *Earth Sci. Rev.* 99 (1–2), 19–30.
- Winguth, A.M.E., et al., 2002. Simulated warm polar currents during the middle Permian. *PALEOCEANOGRAPHY* 17 (4).
- Witkowski, C.R., Weijers, J.W.H., Blais, B., Schouten, S., Sinnighe Damsté, J.S., 2018. Molecular fossils from phytoplankton reveal secular pCO₂ trend over the Phanerozoic. *Science. Advances* 4 (11), eaat4556.
- Wright, J., Schrader, H., Holser, W.T., 1987. Paleoredox variations in ancient oceans recorded by rare earth elements in fossil apatite. *Geochim. Cosmochim. Acta* 51 (3), 631–644.
- Wu, H., Zhang, S., Jiang, G., Huang, Q., 2009. The floating astronomical time scale for the terrestrial late cretaceous Qingshankou Formation from the Songliao Basin of Northeast China and its stratigraphic and paleoclimate implications. *Earth Planet. Sci. Lett.* 278 (3), 308–323.
- Wu, Z., Ren, D., Zhou, H., 2013. Anaerobic Oxidation of methane (AOM) and its Influence on Inorganic Sulfur Cycle in Marine Sediments. *Adv. Earth Science* 28, 765–773.
- Wusiman, J., Zhou, Y.Q., Yao, X., Xu, H.H., Fang, X., 2017. Geochemical characteristics comparison and tectonic background analysis of siliceous rocks from Qixia Formation and Gufeng Formation of Permian in Chaohu Area, Anhui Province. *Geoscience* 31 (4), 734–745.
- Xiong, Y., et al., 2019. Phosphorus cycling in Lake Cadagno, Switzerland: a low sulfate euxinic ocean analogue. *Geochim. Cosmochim. Acta* 251, 116–135.
- Yang, J., Cawood, P.A., Du, Y., Feng, B., Yan, J., 2014. Global continental weathering trends across the early Permian glacial to postglacial transition: Correlating high- and low-paleolatitude sedimentary records. *Geology* 42 (10), 835–838.
- Yao, X., Zhou, Y., Hinnov, L.A., 2015. Astronomical forcing of a Middle Permian chert sequence in Chaohu, South China. *Earth Planet. Sci. Lett.* 422, 206–221.
- Yoshinaga, M.Y., et al., 2014. Carbon isotope equilibration during sulphate-limited anaerobic oxidation of methane. *Nat. Geosci.* 7 (3), 190–194.
- Yu, Y.M., et al., 2021. Upwelling-Induced Organic Matter Enrichment of the Upper Permian Dalong Formation in the Sichuan Basin, SW China and its paleoenvironmental implications, PALAEOGEOGRAPHY PALAECLIMATOLOGY PALAEOECOLOGY, p. 576.
- Yuan, D.-X., et al., 2019. Integrative timescale for the Lopingian (late Permian): a review and update from Shangsi, South China. *Earth Sci. Rev.* 188, 190–209.
- Zabel, M., et al., 2001. Late Quaternary climate changes in Central Africa as inferred from Terrigenous Input to the Niger Fan. *Quat. Res.* 56 (2), 207–217.
- Zhang, B., et al., 2018. Widespread coastal upwelling along the Eastern Paleo-Tethys margin (South China) during the Middle Permian (Guadalupian): Implications for organic matter accumulation. *Mar. Pet. Geol.* 97, 113–126.
- Zhang, B., et al., 2020a. Middle Permian organic carbon isotope stratigraphy and the origin of the Kamura Event. *Gondwana Res.* 79, 217–232.
- Zhang, F.Q., et al., 2020b. Guadalupian (Permian) onset of subduction zone volcanism and geodynamic turnover from passive- to active-margin tectonics in Southeast China. *Geol. Soc. Am. Bull.* 132 (1–2), 130–148.

- Zhang, B., Wignall, P.B., Yao, S., Hu, W., Liu, B., 2021. Collapsed upwelling and intensified euxinia in response to climate warming during the Capitanian (Middle Permian) mass extinction. *Gondwana Res.* 89, 31–46.
- Zhang, B., et al., 2022a. Middle Permian palaeoclimatic-palaeoceanographic evolution and its controls on organic matter accumulation in the lower Yangtze upwelling region. *Int. J. Coal Geol.* 264, 104132.
- Zhang, B., et al., 2022b. New geochemical constraints on the development of active continental margin in Southeast China during the Middle Permian and its tectonic implications. *Gondwana Res.* 103, 458–472.
- Zhang, F., et al., 2022c. Marine anoxia as a trigger for the largest Phanerozoic positive carbon isotope excursion: evidence from carbonate barium isotope record. *Earth Planet. Sci. Lett.* 584, 117421.
- Zhang, J., et al., 2022d. Astronomical forcing of meter-scale organic-rich mudstone-limestone cyclicity in the Eocene Dongying sag, China: Implications for shale reservoir exploration. *AAPG Bull.* 106 (8), 1557–1579.
- Zhang, B., et al., 2023a. The Permian Chert Event in South China: New geochemical constraints and global implications. *Earth Sci. Rev.* 244, 104513.
- Zhang, B., et al., 2023b. Widespread marine euxinia along the western Yangtze Platform caused by oxygen minimum zone expansion during the Capitanian mass extinction. *Glob. Planet. Chang.* 230, 104273.
- Zhao, M.-Y., Zheng, Y.-F., 2015. The intensity of chemical weathering: Geochemical constraints from marine detrital sediments of Triassic age in South China. *Chem. Geol.* 391, 111–122.